ACS OMEGA

http://pubs.acs.org/journal/acsodf

Article

High-Performance, Lightweight, and Flexible Thermoplastic Polyurethane Nanocomposites with Zn^{2+}-Substituted $CoFe_2O_4$ Nanoparticles and Reduced Graphene Oxide as Shielding Materials against Electromagnetic Pollution

Anju, Raghvendra Singh Yadav,* Petra Pötschke, Jürgen Pionteck, Beate Krause, Ivo Kuřitka, Jarmila Vilcakova, David Skoda, Pavel Urbánek, Michal Machovsky, Milan Masař, Michal Urbánek, Marek Jurca, Lukas Kalina, and Jaromir Havlica

Cite This: *ACS Omega* 2021, 6, 28098−28118

Read Online

ACCESS | Metrics & More | Article Recommendations | Supporting Information

ABSTRACT: The development of flexible, lightweight, and thin high-performance electromagnetic interference shielding materials is urgently needed for the protection of humans, the environment, and electronic devices against electromagnetic radiation. To achieve this, the spinel ferrite nanoparticles $CoFe_2O_4$ (CZ1), $Co_{0.67}Zn_{0.33}Fe_2O_4$ (CZ2), and $Co_{0.33}Zn_{0.67}Fe_2O_4$ (CZ3) were prepared by the sonochemical synthesis method. Further, these prepared spinel ferrite nanoparticles and reduced graphene oxide (rGO) were embedded in a thermoplastic polyurethane (TPU) matrix. The maximum electromagnetic interference (EMI) total shielding effectiveness (SE_T) values in the frequency range 8.2−12.4 GHz of these nanocomposites with a thickness of only 0.8 mm were 48.3, 61.8, and 67.8 dB for CZ1-rGO-TPU, CZ2-rGO-TPU, and CZ3-rGO-TPU, respectively. The high-performance electromagnetic interference shielding characteristics of the CZ3-rGO-TPU nanocomposite stem from dipole and interfacial polarization, conduction loss, multiple scattering, eddy current effect, natural resonance, high attenuation constant, and impedance matching. The optimized CZ3-rGO-TPU nanocomposite can be a potential candidate as a lightweight, flexible, thin, and high-performance electromagnetic interference shielding material.

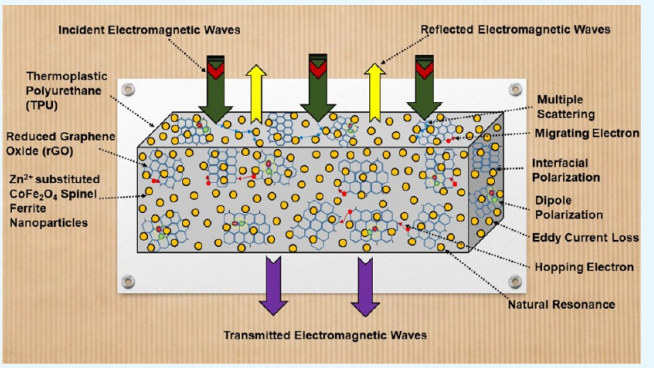

1. INTRODUCTION

In recent years, with the extensive utilization of electrical and electronic appliances, as well as the fast development of information technology, electromagnetic (EM) wave radiation as environmental pollution has received significant attention.[1] Electromagnetic interference (EMI) has affected the working of electronic devices and human health.[2,3] To control such electromagnetic pollution, the development of high-performance electromagnetic shielding material possessing the features of lightweight, flexible, thin, and high absorption characteristics is required. In general, it is noticed that it is difficult for a traditional shielding material to receive satisfactory shielding performance due to the poor impedance matching for the individual magnetic and dielectric electromagnetic wave absorber materials.[4] Consequently, remarkable attempts have been done to create high-performance composite shielding materials consisting of both magnetic and dielectric components, which would provide better impedance matching and enhanced electromagnetic shielding performance through the effective complementarities and synergies between magnetic loss and dielectric loss.[5,6] Further, lightweight and flexible polymer nanocomposites as electromagnetic interference shielding materials have received a lot of attention among researchers due to several other advantages such as corrosion-protection, large-area fabrication, low cost, etc.[7] Polymer nanocomposites with dielectric and magnetic fillers can exhibit fascinating results within the development of high-performance shielding materials. For example, recently, our research group[8,9] reported outstanding lightweight and flexible nanocomposites for electromagnetic interference shielding applications. Further, Han et al.[10] achieved excellent electromagnetic interference shielding characteristics for cellulose-based Ni-decorated graphene magnetic films. Another research group, Acharya et al.,[11] reported an efficient radar absorbing material

Received: August 5, 2021
Accepted: September 30, 2021
Published: October 11, 2021

based on magnetic nanoparticles of a $CuAl_2Fe_{10}O_{19}$-decorated reduced graphene oxide (rGO) filler in a polyvinylidene fluoride matrix. In addition, Fei et al.[12] observed highly efficient electromagnetic interference shielding of Co/C@ cellulose nanofiber aerogels.

Thermoplastic polyurethane (TPU) exhibits excellent mechanical characteristics (tensile strength: ∼58 MPa, elongation at break: ∼1400%, Young's modulus: ∼5−7 MPa, hardness (Shore A ∼72), durability, resistance against chemicals, environmental friendliness, etc.).[13−16] Thermoplastic polyurethane-based EMI shielding materials have several benefits including lightweight, flexibility, easy processability, and resistance to corrosion.[17] Recently, thermoplastic polyurethane has been utilized as a matrix for various nanofillers to develop electromagnetic interference shielding nanocomposites. For example, our research group[18] reported electromagnetic shielding properties of exfoliated graphite (EG)-thermoplastic polyurethane (TPU) nanocomposites with an average shielding effectiveness (SE) value of 20 dB. Jun et al.[19] reported electromagnetic shielding characteristics of graphene nanoribbon (GNR)/thermoplastic polyurethane (TPU) composites. The EMI shielding effectiveness (SE) of the GNR/TPU composite was noticed at 24.9 dB. Further, Shen et al.[20] studied polyurethane/graphene foams as EMI shielding materials and Hsiao et al.[21] studied graphene nanosheet (GN)/waterborne polyurethane (WPU) composites for electromagnetic shielding performance. The EMI SE of GN/WPU composites was 38 dB over the frequency range of 8.2−12.4 GHz. Also, Jia et al.[22] reported an efficient transparent EMI shielding film, consisting of calcium alginate (CA), silver nanowires (AgNW), and polyurethane (PU). The EMI SE of the CA/AgNW/PU film displayed an EMI SE of 20.7 dB. In addition, Menon et al.[23] developed self-healable EMI shielding nanocomposites by cross-linking furfuryl-functionalized reduced graphene oxide (rGO)/Fe_3O_4 with furfuryl-functionalized polyurethane and noticed an EMI SE of 36 dB. Zahid et al.[24] reported nanocomposites based on TPU and rGO for strong EMI shielding applications.

Nanoparticles are preferred for EMI shielding as they have modified magnetic (i.e., superparamagnetism in single-domain nanoparticles) and electrical characteristics in comparison with micron-size nanoparticles.[25] Further, for an effective EMI shielding composite material, the filler size should be comparable or less than the skin depth because of the skin effect.[26,27] Furthermore, the large surface area to volume ratio helps in enhancing interfacial polarization and further EMI shielding.[28,29] Wang et al.[30] noticed that the large-surface-area BN (boron nitride) nanosheets caused abundant interphase interfaces and further increased the interfacial polarization. Graphene is a novel two-dimensional (2D) material obtained from graphite that could generate an abundant dielectric loss. Reduced graphene oxide (rGO) is the reduction product of graphene oxide (GO), which can generate the defect polarization relaxation and functional groups' electronic dipole relaxation and could play an important role in the absorption of electromagnetic waves by EMI shielding materials.[31] According to the previous research literature, the synergistic effect of rGO and magnetic spinel ferrite nanoparticle-based polymer nanocomposites can adjust the impedance matching condition by balancing between complex permeability and permittivity.[32] Further, the magnetic permeability of spinel ferrite nanoparticles can be tuned by controlling its magnetic parameters such as saturation magnetization and coercivity.[33] In this regard, a detailed investigation on the EMI SE performance of nanocomposites with rGO and Zn^{2+}-substituted $CoFe_2O_4$ magnetic spinel ferrite nanoparticles is still missing. Because of this, a lightweight, flexible and high-performance electromagnetic interference shielding nanocomposite has been developed through the investigation of conductivity, dielectric loss, magnetic loss, and impedance matching conditions. It is well known that $CoFe_2O_4$ exhibits a high saturation magnetization and magnetocrystalline anisotropy, which provides higher complex permeability in the higher GHz frequency.[34,35] Further, magnetic and dielectric properties of $CoFe_2O_4$ nanoparticles can be tuned with Zn^{2+} substitution and consequently its microwave absorption characteristics.[36]

In the present work, the impact of Zn^{2+} substitution in $CoFe_2O_4$ spinel ferrite nanoparticles on their structural and magnetic properties was investigated. The substitution of Zn^{2+} with diamagnetic characteristics in $CoFe_2O_4$ spinel ferrite can induce modifications in structural and electromagnetic properties associated with the distribution of cations at octahedral and tetrahedral sites. Furthermore, the impact of Zn^{2+} substitution in $CoFe_2O_4$ spinel ferrite nanoparticles on the electromagnetic interference shielding properties of their nanocomposites with rGO as a second filler and TPU as matrix polymer was investigated. Thermoplastic polyurethane (TPU) was utilized as a polymer matrix because of its flexibility, stretchability, mechanical characteristics, easy processability, and moldability which could easily provide the nanocomposite with flexibility. The potential application of rGO as an EMI shielding material is associated with its extremely high surface area and excellent electrical conductivity. However, due to the nonmagnetic characteristic of rGO, it can only provide high dielectric loss and consequently impedance mismatching issues. The combination of rGO with magnetic spinel ferrite nanoparticles can balance impedance matching conditions. Structural, morphological, and electromagnetic properties of the prepared nanoparticles and their nanocomposites were comprehensively characterized by X-ray diffractometry (XRD), Fourier transfer infrared spectrometry (FTIR), Raman spectrometry, thermogravimetric analysis (TGA), X-ray photoelectron spectroscopy (XPS), transmission electron microscopy (TEM), field emission-scanning electron spectroscopy (FE-SEM), vibrating sample magnetometer (VSM), and a vector network analyzer (VNA). To the best of our knowledge, this is the first detailed study on TPU-based nanocomposites with Zn^{2+}-doped $CoFe_2O_4$ nanoparticles and rGO for electromagnetic interference shielding applications. This study provides the development of high-performance, flexible, lightweight, and thin nanocomposites as potential candidates for electromagnetic interference shielding application.

2. RESULTS AND DISCUSSION

2.1. XRD Study. XRD was applied to study the structure of the prepared nanoparticles and their composites with rGO and TPU. The X-ray diffraction patterns of the prepared CZ1, CZ2, and CZ3 nanoparticles present the characteristic Bragg reflections related to (220), (311), (222), (400), (422), (511), (440), and (533) crystal planes of the cubic spinel ferrite crystal structure belonging to the space group $Fd\bar{3}m$[37] (Figure 1a). Figure 1a displays that all of the samples exhibit the same diffraction peaks. This is due to the successful substitution of Zn^{2+} ions at Co^{2+} in the $CoFe_2O_4$ spinel ferrite crystal

https://doi.org/10.1021/acsomega.1c04192
ACS Omega 2021, 6, 28098−28118

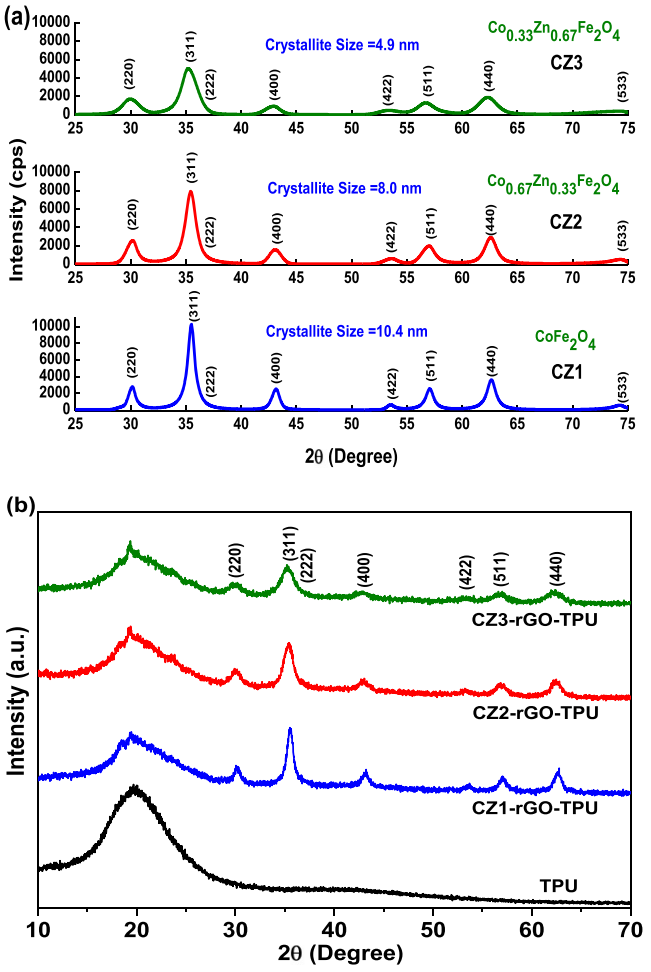

Figure 1. XRD patterns of (a) the prepared CZ1, CZ2, and CZ3 nanoparticles; and (b) thermoplastic polyurethane (TPU) and its nanocomposites CZ1-rGO-TPU, CZ2-rGO-TPU, and CZ3-rGO-TPU.

structure without influencing the crystal structure of cobalt ferrite. Therefore, neither impurities nor a secondary phase is noticeable.[38] The crystallite size of the prepared spinel ferrite nanoparticles is calculated by utilizing Scherrer's formula

$$D = 0.94\lambda/\beta \cos\theta$$

where D is the average crystallite size, λ is the wavelength of Cu Kα radiation, β is the full width at half-maximum intensity for a diffraction peak, and θ is the diffraction angle. The values of estimated crystallite sizes are 10.4, 8.0, and 4.9 nm for CZ1, CZ2, and CZ3 nanoparticles, respectively. The decrease in the crystalline size with the substitution of Zn^{2+} suggests that the presence of Zn^{2+} ions in the synthesis solution has influenced the grain growth of the spinel ferrite nanoparticles.[39] The lattice parameters are calculated by utilizing Bragg's law $d_{hkl} = \frac{\lambda}{2 \sin \theta}$ and $a = d\sqrt{(h^2 + k^2 + l^2)}$. The interplanar spacing d (nm) values indexed using Miller indices (hkl planes) for the prepared nanoparticles are tabulated in Table S1 of the Supporting Information. The lattice parameter a values are 8.376, 8.383, and 8.427 Å for CZ1, CZ2, and CZ3 nanoparticles, respectively.

Figure 1b depicts the XRD pattern of thermoplastic polyurethane (TPU) and its nanocomposites, namely, CZ1-rGO-TPU, CZ2-rGO-TPU, and CZ3-rGO-TPU. It can be noticed that the pure TPU exhibits a broad diffraction peak from 12 to 28°, which is centered at about 2θ = 19.7° of the (110) reflection plane with the interchain spacing of 4.44 Å.[40] This peak is associated with the presence of short-range regular ordered structures of both hard and soft domains along with a disordered structure of the amorphous phase of the TPU.[41] It is also noticeable that this diffraction peak is broadened and reduced in intensity with the addition of nanofillers (spinel ferrite nanoparticles and rGO) into the TPU, which signifies that the nanofillers considerably influence the short-range microstructural orders of hard and soft segments of the TPU. Further, the XRD peaks indexed as (220), (311), (222), (400), (422), (511), and (440) approve the presence of spinel ferrite nanoparticles in the TPU matrix.[42] Furthermore, no separate diffraction peaks of rGO were noticed, which is associated with its fine dispersion and small size.[9]

2.2. Raman Spectroscopy. The Raman spectra of the prepared spinel ferrite nanoparticles revealed Raman bands at 166−183 cm^{-1} ($T_{2g}(1)$), 292−330 cm^{-1} (E_g), 466−481 cm^{-1} ($T_{2g}(2)$), 546−580 cm^{-1} ($T_{2g}(3)$), 612−620 cm^{-1} ($A_g(2)$), and 666−677 cm^{-1} ($A_g(1)$)[43] (Figure 2a). The Raman spectra of graphene oxide (GO) and reduced graphene oxide (rGO) are depicted in Figure 2b. The D-band is associated with the defect-induced breathing mode of A_{1g} symmetry and the G-band is related to the E_{2g} symmetry attributed to the relative degree of graphitization.[44] It can be noticed that the Raman spectrum of rGO exhibits two major Raman bands, i.e., the D-band at 1347 cm^{-1} and G-band at 1576 cm^{-1}. For GO, the D-band and G-band are noticed at 1353 and 1593 cm^{-1}, respectively.[45] The ratio of the intensity of the D- and G-bands was 1.19 and 1.0 for rGO and GO, respectively. The increased intensity of the D-band in contrast with the G-band in rGO compared to GO is associated with the increase of defects in the carbon lattice with reduction or increased number of polyaromatic domains with a decreased overall size in rGO.[46] The 2D band at 2684 $cm^{-1}$and the D + G band at 2915 cm^{-1} for rGO were also noticed. The 2D band is associated with inelastic scattering from two phonons; however, the D + G band is associated with the result of a combination of both D-band and G-band.[47]

The Raman spectra of TPU and its nanocomposites CZ1-rGO-TPU, CZ2-rGO-TPU, and CZ3-rGO-TPU are depicted in Figure 2c,d, at laser excitation wavelengths of 532 and 780 nm. The main characteristics of the Raman peaks of TPU at 2925, 1726, 1616, 1542, and 1441 cm^{-1} are associated with the stretching vibration of $-CH_2$, the free carbonyl group, aromatic breathing mode of vibration of C═C, the vibration of C═C of urethane amide, and the bending vibration of $-CH_2$, respectively.[48] The intensity of these peaks is decreased with the addition of nanofillers in TPU, which can be attributed to the interaction of these nanofillers with TPU.[49] The featured Raman peaks of rGO in the prepared nanocomposites are noticed at 1347 and 1576 cm^{-1} corresponding to D- and G-bands, respectively. Further, the peaks of spinel ferrite in the nanocomposites are noticed at 466, 612, and 668 cm^{-1} and are associated with $T_{2g}(2)$, $A_g(2)$, and $A_g(1)$, respectively.

2.3. FTIR Spectroscopy. Infrared spectroscopy is utilized to investigate the presence of different vibrational modes associated with the metal ions in the crystal lattice.[50] Figure 3a depicts the FTIR spectra of the prepared spinel ferrite nanoparticles CZ1, CZ2, and CZ3. The presence of two characteristics FTIR bands can be seen. The band noticed in

https://doi.org/10.1021/acsomega.1c04192
ACS Omega 2021, 6, 28098−28118

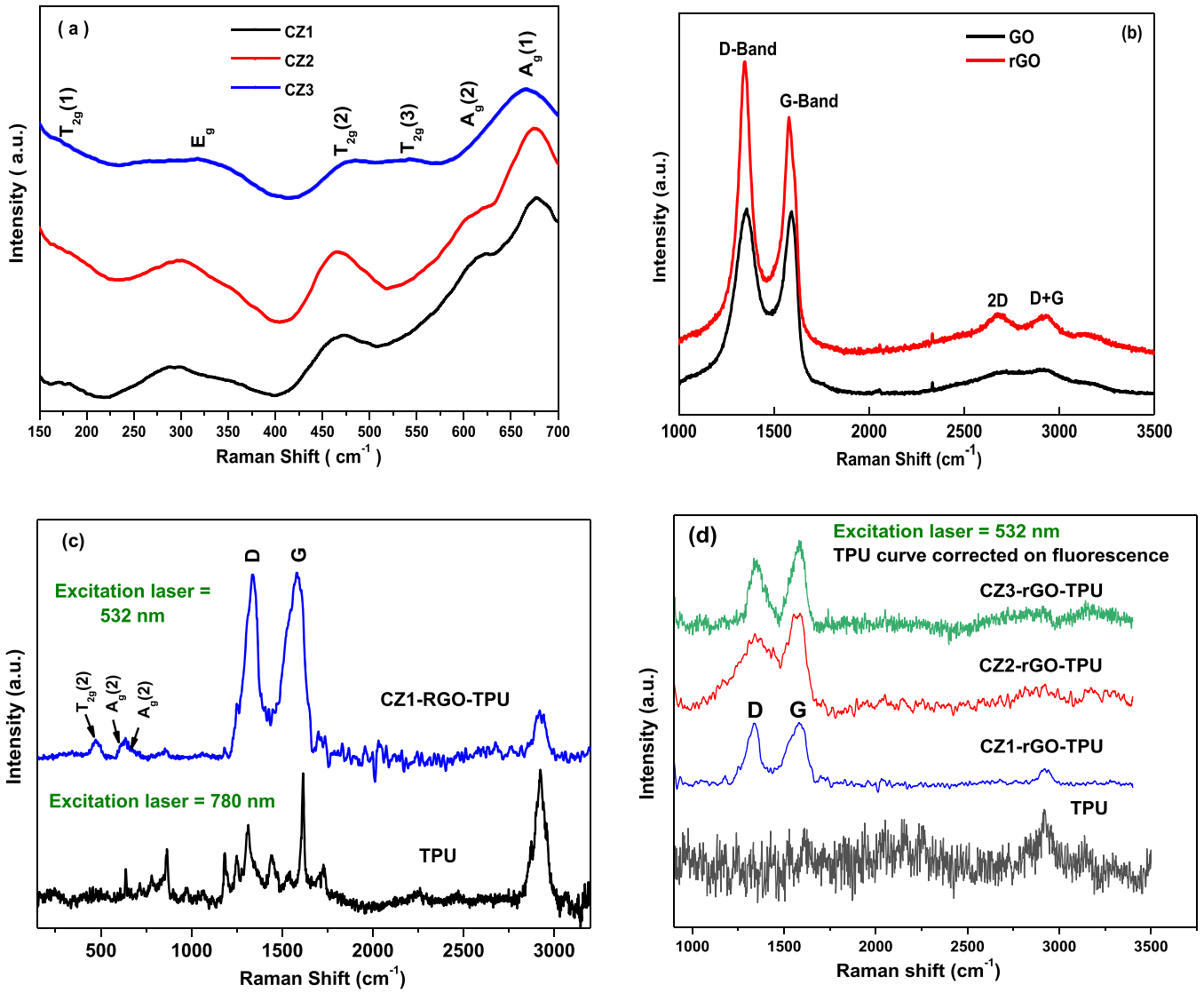

Figure 2. Raman spectra of (a) the prepared CZ1, CZ2, and CZ3 samples; (b) graphene oxide (GO) and reduced graphene oxide (rGO); and (c, d) TPU and its nanocomposites CZ1-rGO-TPU, CZ2-rGO-TPU, and CZ3-rGO-TPU.

the lower frequency range 295−301 cm^{-1} is associated with the intrinsic vibrations of the octahedral sites. The observed band at a higher frequency range of 532−548 cm^{-1} is related to the intrinsic vibrations of the tetrahedral sites. The observed two absorption bands signify the single-phase spinel ferrite structure, which has two sublattices, the tetrahedral (A) site and octahedral (B) site.[51] The shift in the absorption band position was noticed in the prepared spinel ferrite nanoparticles. It was associated with cation redistribution at the tetrahedral (A) site and octahedral (B) site, as noticed in the XPS study (Figure S1) (Supporting Information).[52] By the XPS study, the occupation formula was $(Co^{2+}_{0.24}Fe^{3+}_{0.92})[Co^{2+}_{0.76}Fe^{3+}_{1.08}]O_4$, $(Co^{2+}_{0.26}Zn^{2+}_{1.00}Fe^{3+}_{0.88})[Co^{2+}_{0.74}Fe^{3+}_{1.12}]O_4$ and $(Co^{2+}_{0.30}Zn^{2+}_{0.54}Fe^{3+}_{1.24})[Co^{2+}_{0.70}Zn^{2+}_{0.46}Fe^{3+}_{0.76}]O_4$ for CZ1, CZ2, and CZ3 samples, respectively. Further, detailed XPS study (Figure S2) of GO and rGO is mentioned in Supporting Information.

FTIR spectroscopy is also utilized to investigate the functional groups that are present in GO and rGO (Figure 3b). The FTIR spectra of GO exhibit a strong and broad absorption band at 3303 cm^{-1}, which is associated with hydroxyl (O−H) stretching vibrations. The absorption bands at 1714, 1611, 1401, 1165, and 1034 cm^{-1} are associated with stretching vibrations of the carboxyl (C═O), sp^2-hybridized C═C, deformation vibration of hydroxyl (O−H), stretching vibrations of alcoholic (C−OH), and C−O stretching vibration of epoxy, respectively.[53,54] The FTIR spectrum of rGO exhibits reduced intensity or even elimination of the typical bands representing these functional groups, which confirms the successful reduction of GO into rGO.[55]

FTIR spectra of TPU and its nanocomposites, namely CZ1-rGO-TPU, CZ2-rGO-TPU, and CZ3-rGO-TPU, are depicted in Figure 3c. The presence of absorption peaks at 3331, 1726, and 1706 cm^{-1} is associated with the hydrogen-bonded N−H stretching, free and hydrogen-bonded C═O stretching of TPU, respectively.[56] The absorption peaks at 1530, 1221, 1142, 2868, and 2951 cm^{-1} are related to C−N stretching, alkoxy C−O stretching, epoxy O−C−O stretching, symmetric CH_2 stretching, and asymmetric CH_2 stretching of TPU.[57,58] The prepared nanocomposites based on TPU also exhibited these observed absorption peaks, which are expected when nanocomposites with nonreacting fillers are formed.

https://doi.org/10.1021/acsomega.1c04192
ACS Omega 2021, 6, 28098−28118

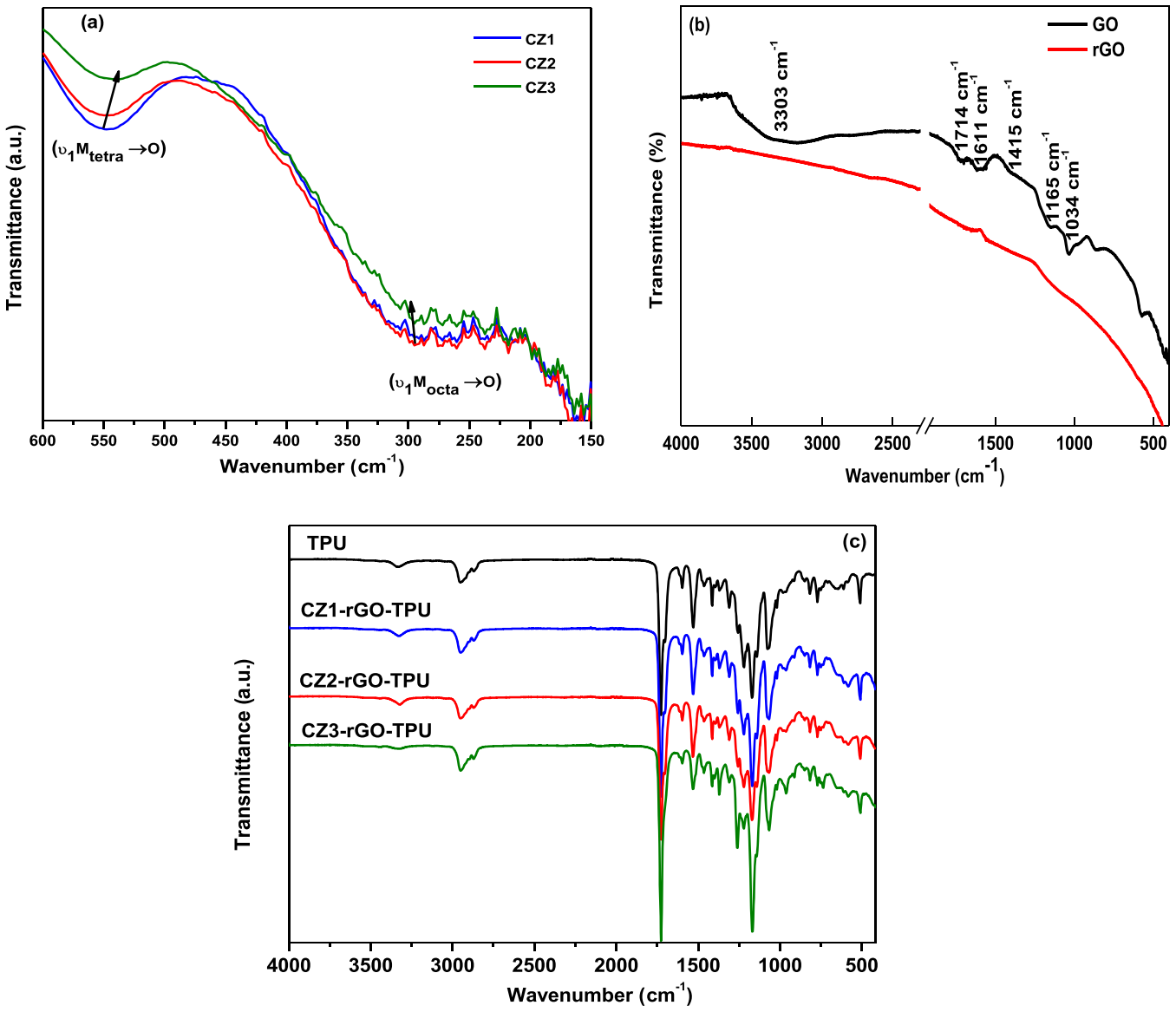

Figure 3. FTIR spectra of (a) the prepared CZ1, CZ2, and CZ3 nanoparticles; (b) graphene oxide (GO) and reduced graphene oxide (rGO); and (c) TPU and its nanocomposites CZ1-rGO-TPU, CZ2-rGO-TPU, and CZ3-rGO-TPU.

2.4. TEM Study of the Prepared Nanoparticles. Figure 4 depicts TEM and high-resolution TEM (HRTEM) images of the prepared magnetic spinel ferrite nanoparticles, i.e., CZ1, CZ2, and CZ3. A representative TEM image of the CZ1 sample is shown in Figure 4a, which refers to nanoparticles with sizes in the range of 7−15 nm. A typical HRTEM image of the CZ1 sample is shown in Figure 4b. The observation of lattice fringes represents the formation of good crystalline spinel ferrite nanoparticles. The measured distance of 0.25 nm is associated with d_{hkl} of the (311) planes of the spinel ferrite crystal structure.[59] Further, Figure 4c depicts a representative TEM image of the CZ2 sample, which signifies spherical nanoparticles with sizes in the range of 5−9 nm. The periodic lattice fringe spacing of 0.29 nm corresponding to the (220) plane of the spinel ferrite structure can be noticed in Figure 4d.[60]

Furthermore, a typical TEM image of the CZ3 sample is shown in Figure 4e, which represents spherical nanoparticles with sizes in the range of 3−6 nm. The distinct lattice fringes with a spacing of 0.25 nm corresponding to the (311) planes of cubic spinel ferrite can be observed in Figure 4f.

2.5. FE-SEM Study of Nanoparticles and Nanocomposites. Figure 5a shows a representative FE-SEM image of the prepared GO, which represents the dense stacking of GO sheets. A typical FE-SEM image of the developed rGO is shown in Figure 5b, which exhibits a wrinkled, fluffy, and disordered morphology. The cross-sectional view of the prepared nanocomposites was investigated to obtain information about the distribution and dispersion of the spinel ferrite nanoparticles and rGO within the TPU nanocomposite samples. Figure 6a−c depicts the FE-SEM images of the fractured surfaces of TPU-based nanocomposites containing spinel ferrite nanoparticles (CZ1 or CZ2 or CZ3, respectively) and rGO, which represent the good distribution of the spinel ferrite nanoparticles and random distribution of the larger rGO sheetlike structures in the TPU matrix. In addition, some additional FE-SEM images of the fractured surfaces of CZ3-RGO-TPU nanocomposites are shown in Figure S3a,b of the Supporting Information. The

https://doi.org/10.1021/acsomega.1c04192
ACS Omega 2021, 6, 28098−28118

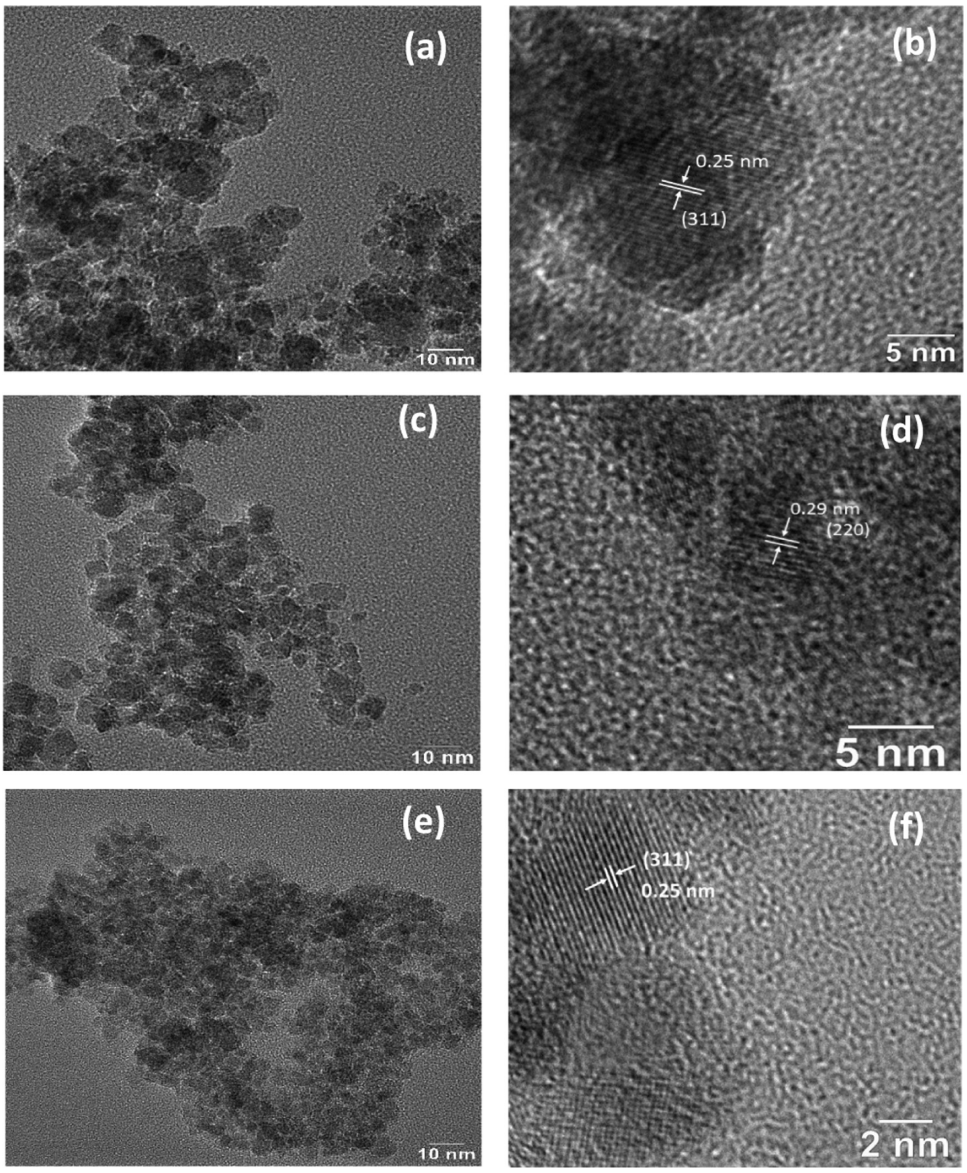

Figure 4. (a) TEM image of CZ1, (b) HRTEM image of CZ1, (c) TEM image of CZ2, (d) HRTEM image of CZ2, (e) TEM image of CZ3, and (f) HRTEM image of CZ3.

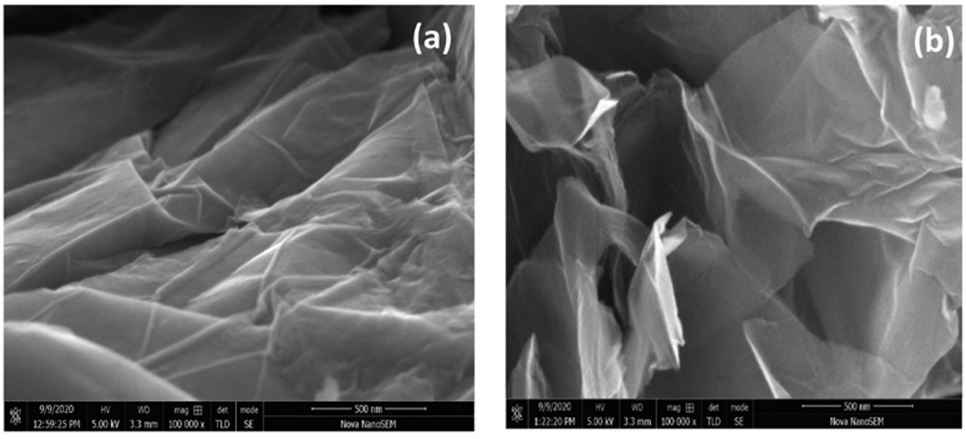

Figure 5. FE-SEM images of (a) GO and (b) rGO.

energy-dispersive X-ray (EDX) spectrum of the CZ3-rGO-TPU nanocomposite sample verifies the presence of the elements C, O, Co, Fe, and Zn in the nanocomposite sample (Figure 6d). The portion of the SEM image, which was utilized

https://doi.org/10.1021/acsomega.1c04192
ACS Omega 2021, 6, 28098−28118

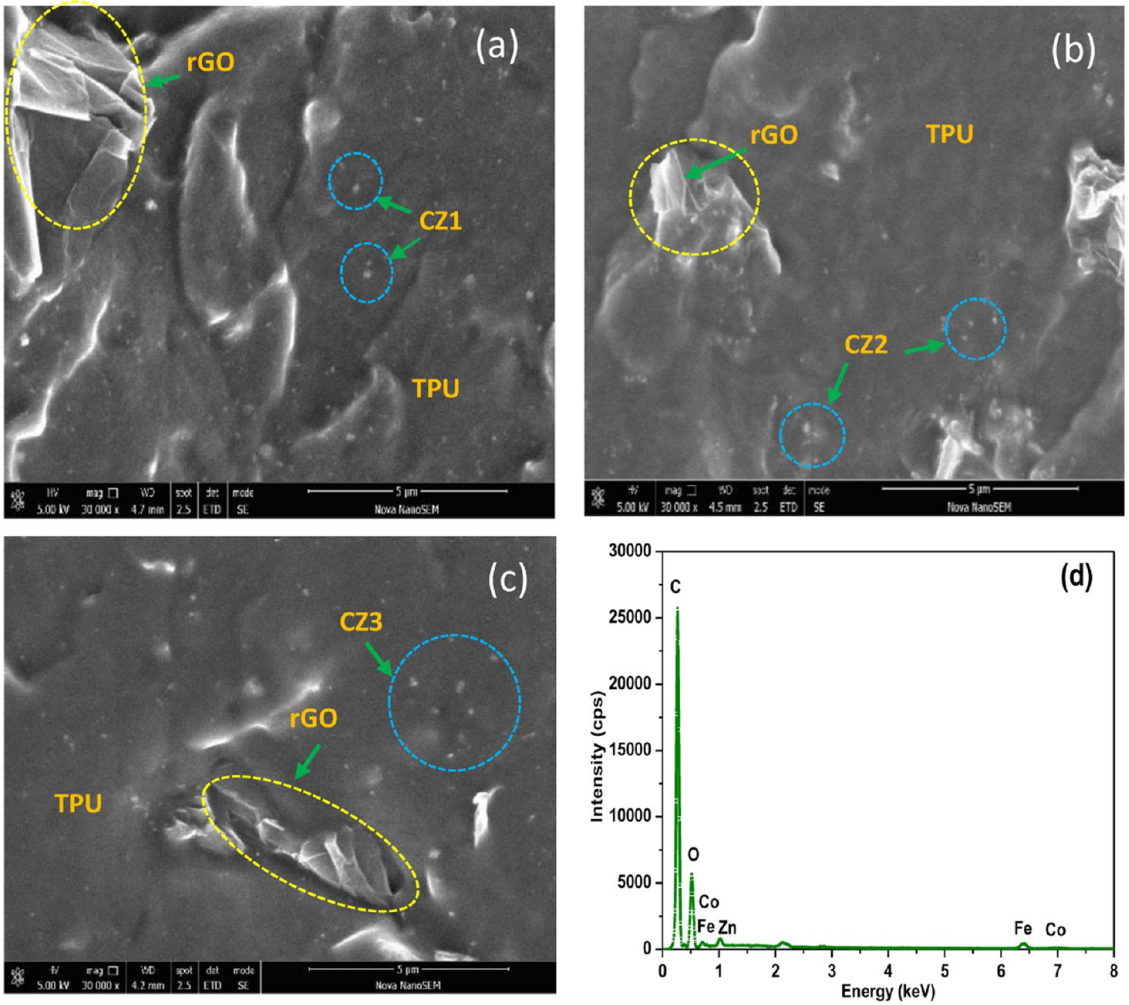

Figure 6. FE-SEM images of the fracture surface of (a) CZ1-rGO-TPU, (b) CZ2-rGO-TPU, (c) CZ3-rGO-TPU, and (d) the EDX spectrum of CZ3-rGO-TPU.

for the EDX study, is shown in Figure S3c of the Supporting Information. Furthermore, the elemental mapping image of the CZ2-rGO-TPU nanocomposite is shown in Figure S4 of the Supporting Information. The results display that Co, Fe, Zn, and O are distributed uniformly, which further proves the good dispersion of ferrite in the TPU matrix. In addition, thermogravimetric analyses (TGA) of TPU and the prepared nanocomposites (Figure S5) are also added in the Supporting Information.

2.6. Magnetic Properties. The magnetic properties of the prepared nanoparticles were investigated utilizing a vibrating sample magnetometer (VSM) at room temperature in an applied magnetic field up to 10 kOe. The saturation magnetization values are 51.7, 49.7, and 14.5 emu/g for CZ1, CZ2, and CZ3 samples, respectively (Figure 7). The decrease in the saturation magnetization value is associated with the doping of the nonmagnetic Zn^{2+} ion in $CoFe_2O_4$ spinel ferrite nanoparticles as well as the decrease in the particle size of the doped spinel ferrite nanoparticles.[61] The prepared CZ1 sample exhibits the coercivity of $H_c \approx 73$ Oe and the remanent magnetization of $M_r = 4.7$ emu/g, which signifies the ferromagnetic behavior. Further, due to the low values of coercivity H_c (≈1.3 Oe for CZ2 and 0 for CZ3) and remanent magnetization M_r (0.12 for CZ2 and 0 for CZ3), the prepared CZ2 and CZ3 nanoparticles exhibited super-

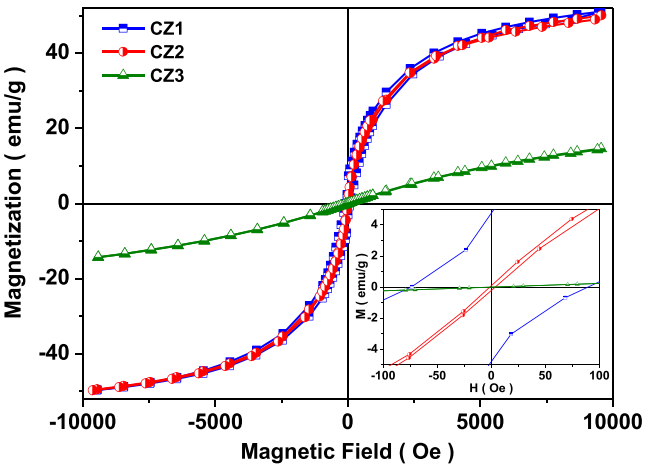

Figure 7. Magnetic hysteresis curves of the prepared CZ1, CZ2, and CZ3 nanoparticles.

paramagnetic characteristics.[62] This indicates that with the addition of Zn^{2+} there is the transformation of ferromagnetic characteristics to superparamagnetism due to a decreased crystallite size in the presence of Zn^{2+} ions, which hamper the crystal growth in the synthesis process.[63] It can be proposed that the nanocomposite based on CZ3 could be a better

https://doi.org/10.1021/acsomega.1c04192
ACS Omega 2021, 6, 28098−28118

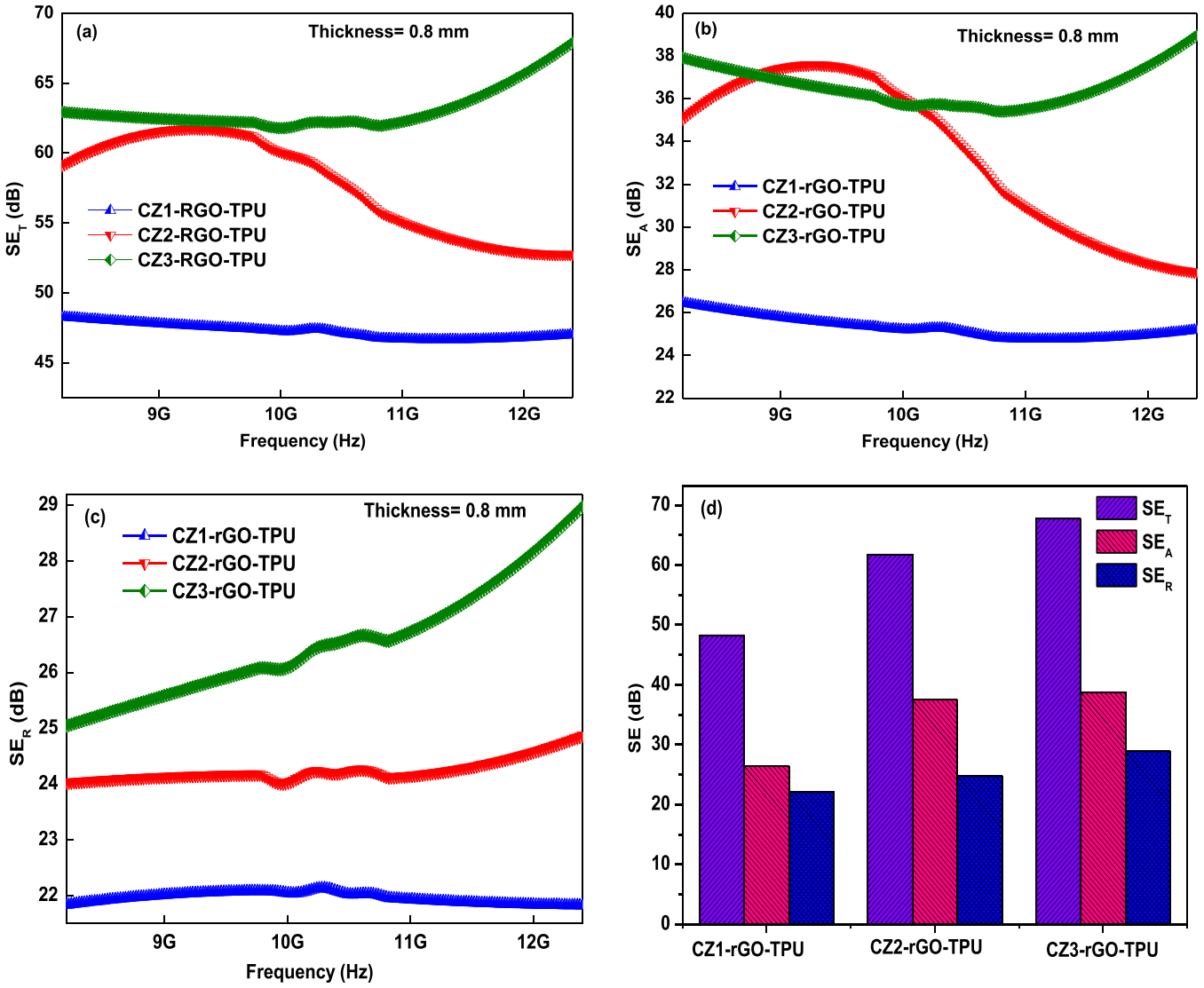

Figure 8. (a) Total shielding effectiveness SE_T, (b) shielding effectiveness due to absorption SE_A, (c) shielding effectiveness due to reflection SE_R, and (d) comparison chart of the maximum values of SE_T, SE_A, and SE_R for the prepared nanocomposites CZ1-rGO-TPU, CZ2-rGO-TPU, and CZ3-rGO-TPU with a thickness of 0.8 mm.

electromagnetic wave absorbing material due to higher anisotropy energy (H_a), which can be expressed by the relation[64,65]

$$H_a = 4|K_1|/3\mu_o M_s$$

where $|K_1|$ is the anisotropy coefficient. The anisotropic energy of CZ3 is higher as it exhibits a lower M_S value. The evaluated values of anisotropy energy are 86, 90, and 311 kOe for CZ1, CZ2, and CZ3 samples, respectively.[66,67]

2.7. Electromagnetic Interference Shielding Effectiveness of the Nanocomposites. The total shielding effectiveness (SE_T) of the material against EMI can be defined by its ability to attenuate electromagnetic waves and is expressed in decibel (dB) units.[68] The high value of EMI SE (dB) of a shielding material signifies less transmission of EM waves through the shielding material. The total EMI shielding effectiveness (SE_T) can be expressed by the following relation in terms of the logarithm of the ratio of the incident power (P_I) to the transmitted power (P_T)[69]

$$SE_T(\text{dB}) = 10 \log\left(\frac{P_I}{P_T}\right)$$

In general, when the incident electromagnetic waves interact with the shielding material, the incident power can be divided into reflected power, absorbed power, and transmitted power. Therefore, the total EMI shielding effectiveness (SE_T) includes the contribution of reflection (SE_R), absorption (SE_A), and multiple internal reflections (SE_M), which can be expressed as[70]

$$SE_T = SE_R + SE_A + SE_M$$

The multiple internal reflection (SE_M) terms can be ignored where the contribution of absorption to the total EMI shielding effectiveness (SE_T) is more than 10 dB or when the shielding material thickness is greater than the skin depth.[71] Therefore, SE_T can be expressed as

$$SE_T = SE_R + SE_A$$

https://doi.org/10.1021/acsomega.1c04192
ACS Omega 2021, 6, 28098−28118

Table 1. Electromagnetic Shielding Performance of Some Nanocomposites Reported in the Literature

no.	shielding material	frequency (GHz)	specimen thickness	maximum value of SE_T (dB)	ref
1	MWNTs + rGO-Fe_3O_4 in polycarbonate (PC)/poly(styrene-*co*-acrylonitrile) (SAN) blend	8−18	0.92 mm	50.7	77
2	rGO-$MnFe_2O_4$ + MWCNTs in PVDF	2−18	5.5 mm	38	78
3	TPU/PLA/VCB	8.2−12.4	1.0 mm	27	79
4	TPU/CoFe/coal fly ash	0.1−20	250 μm	37	80
5	PTH/$Ni_{0.5}Zn_{0.5}Fe_{2-x}Ce_xO_4$	8.2−12.4	2.0 mm	34	81
6	TPU/rGO	0.1−20	250 μm	53	24
7	rGO/PS	8.2−12.4	2.5 mm	45.1	82
8	polypyrrole/BST/rGO/Fe_3O_4	8.2−12	2.5 mm	48.6	83
9	$Co_{0.33}Zn_{0.67}Fe_2O_4$-rGO-TPU	8.2−12.4	0.8 mm	67.8	this work

The shielding effectiveness due to reflection (SE_R) is associated with the impedance mismatch between air and the shielding material; however, the shielding effectiveness due to absorption (SE_A) is related to the energy dissipation of the electromagnetic waves in the shielding material.[72]

The total EMI shielding effectiveness (SE_T) can be evaluated using the following relations in terms of the scattering parameters obtained from the vector network analyzer[73]

$$SE_T(dB) = 10\log_{10}\left(\frac{1}{S_{12}^2}\right) = 10\log_{10}\left(\frac{1}{S_{21}^2}\right)$$

$$SE_R(dB) = 10\log_{10}\left(\frac{1}{1 - S_{11}^2}\right)$$

$$SE_A(dB) = 10\log_{10}\left(\frac{1 - S_{11}^2}{S_{12}^2}\right)$$

where S_{11}, S_{12}, S_{21}, and S_{22} represent the forward reflection coefficient, forward transmission coefficient, backward transmission coefficient, and reverse reflection coefficient, respectively.

The total shielding effectiveness (SE_T) of the prepared TPU-based nanocomposites is depicted in Figure 8a in the frequency range of 8.2−12.4 GHz for a sample thickness of 0.8 mm. The maximum values of SE_T are 48.3, 61.8, and 67.8 dB for CZ1-rGO-TPU, CZ2-rGO-TPU, and CZ3-rGO-TPU, respectively. Figure 8b,c depicts the shielding effectiveness due to absorption (SE_A) and due to reflection (SE_R), respectively. The maximum values of SE_A are 26.4, 37.5, and 38.8 dB; and the maximum values of SE_R are 22.1, 24.8, and 28.9 dB for CZ1-rGO-TPU, CZ2-rGO-TPU, and CZ3-rGO-TPU, respectively. Figure 8d shows a comparison chart of SE_T, SE_A, and SE_R for the prepared nanocomposites CZ1-rGO-TPU, CZ2-rGO-TPU, and CZ3-rGO-TPU with a thickness of 0.8 mm. It is noticed that the prepared nanocomposites have absorption-dominant EMI shielding behavior.

The value of EMI SE higher than 20 dB is considered the least target value for commercial applications such as in aircraft, satellite, telecommunications, and defense systems.[74] It is well known that the shielding material having 20 dB of EMI SE is capable to block 99% of incident electromagnetic waves with less than or equal to 1% transmission of electromagnetic waves. The EMI shielding efficiency (%), which represents the percentage of the blocked electromagnetic waves by the shielding material, can be evaluated using the following relation with the EMI shielding effectiveness (dB)[75]

$$\text{shielding efficiency (\%)} = 100 - \left(\frac{1}{10^{SE/10}}\right) \times 100$$

Importantly, the shielding efficiency of the CZ3-rGO-TPU nanocomposite was up to 99.9999%, which signifies a blockage of 99.9999% of the incident electromagnetic wave with only 0.0001% transmission. In comparison with conventional metal-based EMI shielding material, which has no electromagnetic wave absorption ability, the prepared TPU-based nanocomposites with spinel ferrite nanoparticles and reduced graphene oxide feature a compatible shielding mechanism of absorption and reflection to incident electromagnetic waves and provide benefits of a lightweight, flexible, and high-performance shielding effectiveness.[76] In addition, the developed absorption-dominant EMI shielding material minimizes the second harm created by the reflected electromagnetic waves, and it has its place in an eye-catching environmentally friendly shielding material.

The related recent work by other researchers on the electromagnetic shielding performance of nanocomposites is included in Table 1. The group of Pawar et al.[77] measured a total shielding effectiveness value of SE_T of ∼50.7 dB at 18 GHz for polycarbonate (PC)/poly(styrene-*co*-acrylonitrile) (SAN) blend samples containing both multiwalled carbon nanotubes (MWNTs) and rGO-Fe_3O_4 having a thickness of 0.92 mm. Further, a total shielding effectiveness value of SE_T of ∼38 dB at 18 GHz is reported by the group of Srivastava et al.[78] for rGO-$MnFe_2O_4$-multiwalled carbon nanotube (MWCNT)-poly(vinylidene fluoride) (PVDF) composite samples with a thickness of 5.5 mm. Furthermore, Nath et al.[79] showed a maximum shielding effectiveness of ∼27 dB in the frequency range 8.2−12.4 GHz, thermoplastic polyurethane (TPU)/polylactic acid(PLA)/conductive carbon black Vulcan XC-72 (VCB) nanocomposites with a thickness of 1 mm. Gulzar et al.[80] observed a SE_T value of ∼37 dB in the microwave region for samples possessing 250 μm thickness for TPU/CoFe/coal fly ash nanocomposites. Also, Dar et al.[81] reported the total shielding effectiveness of ∼34 dB for polythiophene/$Ni_{0.5}Zn_{0.5}Fe_{2-x}Ce_xO_4$ nanocomposites, whereas Zahid et al.[24] noticed that the shielding effectiveness for the composite of 2.5% rGO loading was ∼53 dB in the frequency range 0.1−20 GHz. Another group of Yan et al.[82] reported the maximum shielding effectiveness of ∼45.1 dB for structured reduced graphene oxide/polymer composites (rGO/PS) with a sample thickness of 2.5 mm in the X-band frequency range. Also, Sambyal et al.[83] noticed a total shielding effectiveness value, SE_T ∼48.6 dB, for the polypyrrole/BST/RGO/Fe_3O_4 composite with a thickness of 2.5 mm in the X-band frequency region.

https://doi.org/10.1021/acsomega.1c04192
ACS Omega 2021, 6, 28098−28118

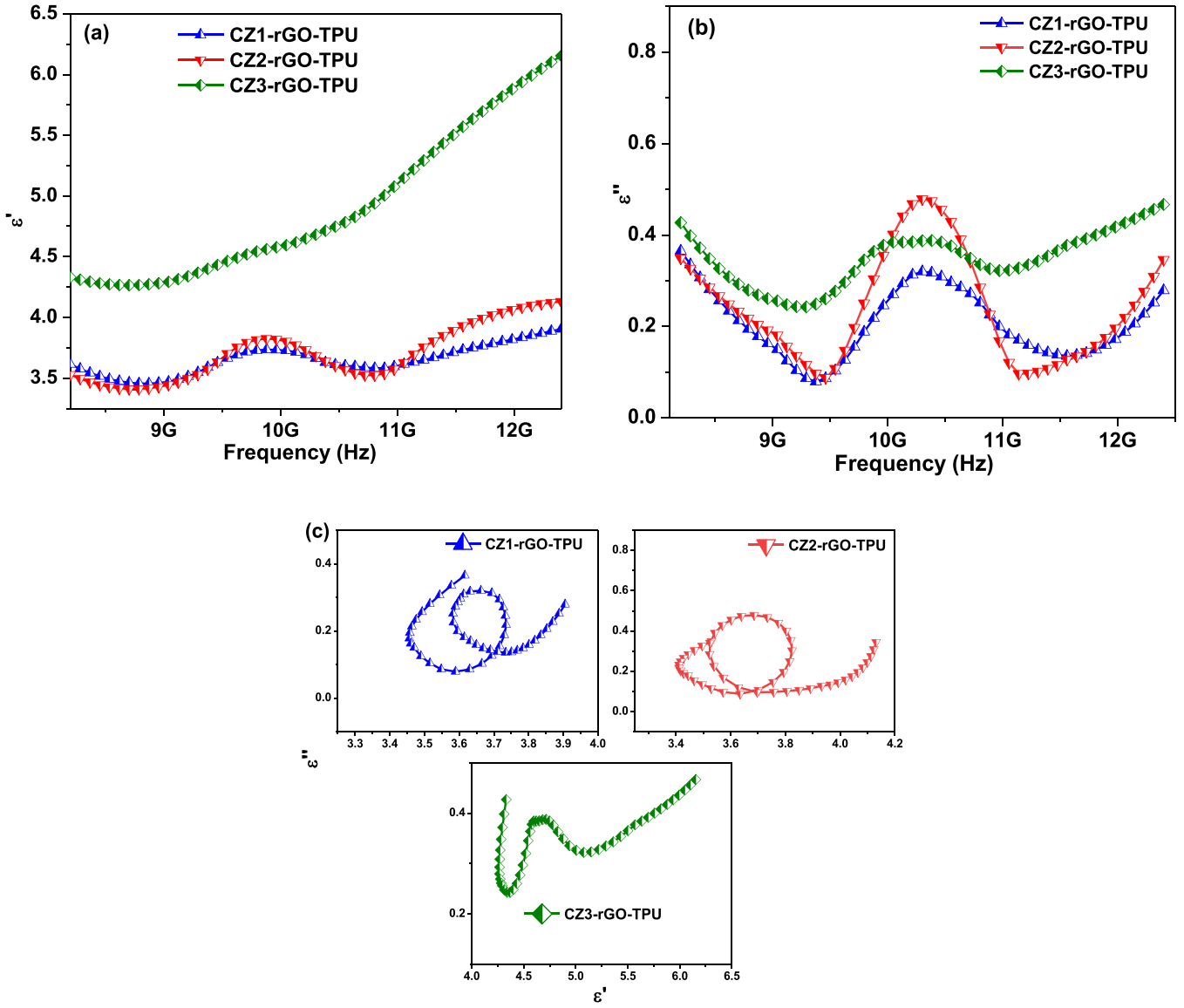

Figure 9. (a) Real part of permittivity, (b) imaginary part of permittivity, and (c) Cole−Cole plots of CZ1-rGO-TPU, CZ2-rGO-TPU, and CZ3-rGO-TPU nanocomposites.

Lightweightness is one of the most essential benefits for shielding materials, particularly for applications in aircraft, satellite, and defense systems where the weight of the shielding material is a significant design parameter. Taking the density of the shielding material into account, the specific shielding effectiveness (SSE) is evaluated by dividing the SE by density. Further, absolute shielding effectiveness (SSE_t) is obtained by dividing SSE by the thickness (t) of the shielding material.[84] The thickness of each nanocomposite is 0.8 mm and the density is in the range of 0.80−1.17 g/cm^3. The evaluated value of SSE for nanocomposites is in the range of 53.5−78 dB cm^3/g, which is much larger than that of typical metals, for example, ∼10 dB cm^3/g for solid copper.[85] The calculated value of SSE_t for nanocomposites is in the range of 668−963 dB cm^2/g. A research group of Liu et al.[86] observed the SSE value of 37.03 dB cm^3/g for three-dimensional (3D) network porous graphene nanoplatelets/Fe_3O_4/epoxy nanocomposites. Further, Zhang et al.[87] noticed the value of SSE ∼ 17−25 dB cm^3/g for poly(methyl methacrylate) (PMMA)/graphene nanocomposite. Furthermore, Shen et al.[88] demonstrated the value of SSE ∼ 41.5 dB cm^3/g for polyetherimide/graphene@Fe_3O_4 composite. For PMMA/Fe_3O_4@MWCNT nanocomposite, the value of SSE ∼ 50 dB cm^3/g was noticed by the research team of Zhang et al.[89] In addition, Ling et al.[90] observed the value of SSE ∼ 44 dB cm^3/g for the polyetherimide/graphene composite.

2.8. Electromagnetic Properties and Parameters of the Nanocomposites. The shielding material with very high electrical conductivity and consisting of free charge carriers are effective electromagnetic wave reflectors. Further, to absorb electromagnetic waves, the shielding materials should exhibit electric and magnetic dipoles. The magnitude of the shielding effectiveness by reflection (SE_R), which has a dependence on the conductivity and permeability, can be evaluated theoretically using the following relation[91]

$$SE_R = -10 \log_{10}\left(\frac{\sigma_T}{16\omega\varepsilon_o\mu_r}\right)$$

https://doi.org/10.1021/acsomega.1c04192
ACS Omega 2021, 6, 28098−28118

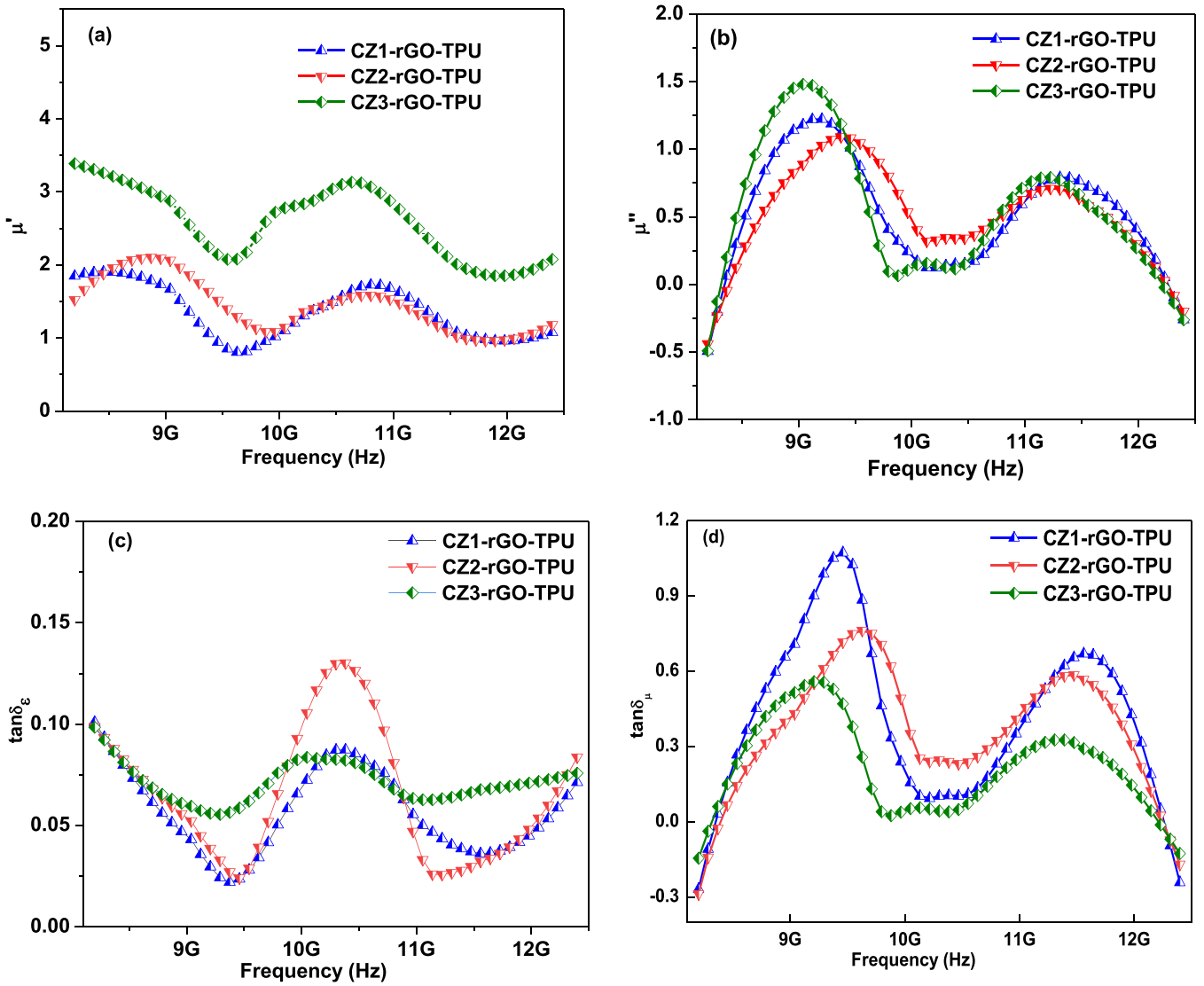

Figure 10. (a) Real part (μ') of permeability, (b) imaginary part (μ'') of permeability, (c) dielectric loss (tan δ_ε), and (d) magnetic loss (tan δ_μ) of CZ1-rGO-TPU, CZ2-rGO-TPU, and CZ3-rGO-TPU nanocomposites.

where σ_T represents the total conductivity of the shielding material and μ_r corresponds to the relative permeability of the shielding material. The above equation signifies that the value of SE_R is higher for larger conductivity and lower magnetic permeability of the shielding material. The magnitude of the shielding effectiveness by absorption (SE_A) can be also evaluated theoretically by the following equation[91]

$$SE_A = -8.68t\left(\frac{\sigma_T \omega \mu_r}{2}\right)^{1/2}$$

where t is the thickness of shielding material. The above equation represents that the SE_A is larger with high electrical conductivity and high magnetic permeability of the shielding material. The electromagnetic wave absorption can be also improved by the increase of the thickness of the shielding material. In addition, to investigate the reason behind the noticed improvement in the EMI SE in developed nanocomposites, the electromagnetic parameters such as permittivity, permeability, conductivity, polarization, dielectric loss, magnetic loss, skin depth, eddy current loss, natural resonance, attenuation constant, and impedance matching have been investigated.

The real part (ε') of permittivity signifies the storage ability of electric energy. Figure 9a depicts the real part (ε') of permittivity with the variation of frequency of the prepared nanocomposites CZ1-rGO-TPU, CZ2-rGO-TPU, and CZ3-rGO-TPU. The values of ε' are in the ranges of 3.4−3.9, 3.4−4.1, and 4.2−6.1 for CZ1-rGO-TPU, CZ2-rGO-TPU, and CZ3-rGO-TPU, respectively. The ε' is associated with the polarization of the material, which includes dipolar polarization, electric polarization, orientation polarization, and interfacial polarization under electromagnetic waves. Because of the residual bonds and defects created during the chemical synthesis process, electrons are not homogeneously distributed, which provides orientation polarization and further plays a role in the ε'.[92] In the developed nanocomposites, the presence of interfaces between the spinel ferrite nanoparticles and rGO sheets in the TPU matrix provides interfacial polarization, also known as the Maxwell−Wagner polarization.[93]

https://doi.org/10.1021/acsomega.1c04192
ACS Omega 2021, 6, 28098−28118

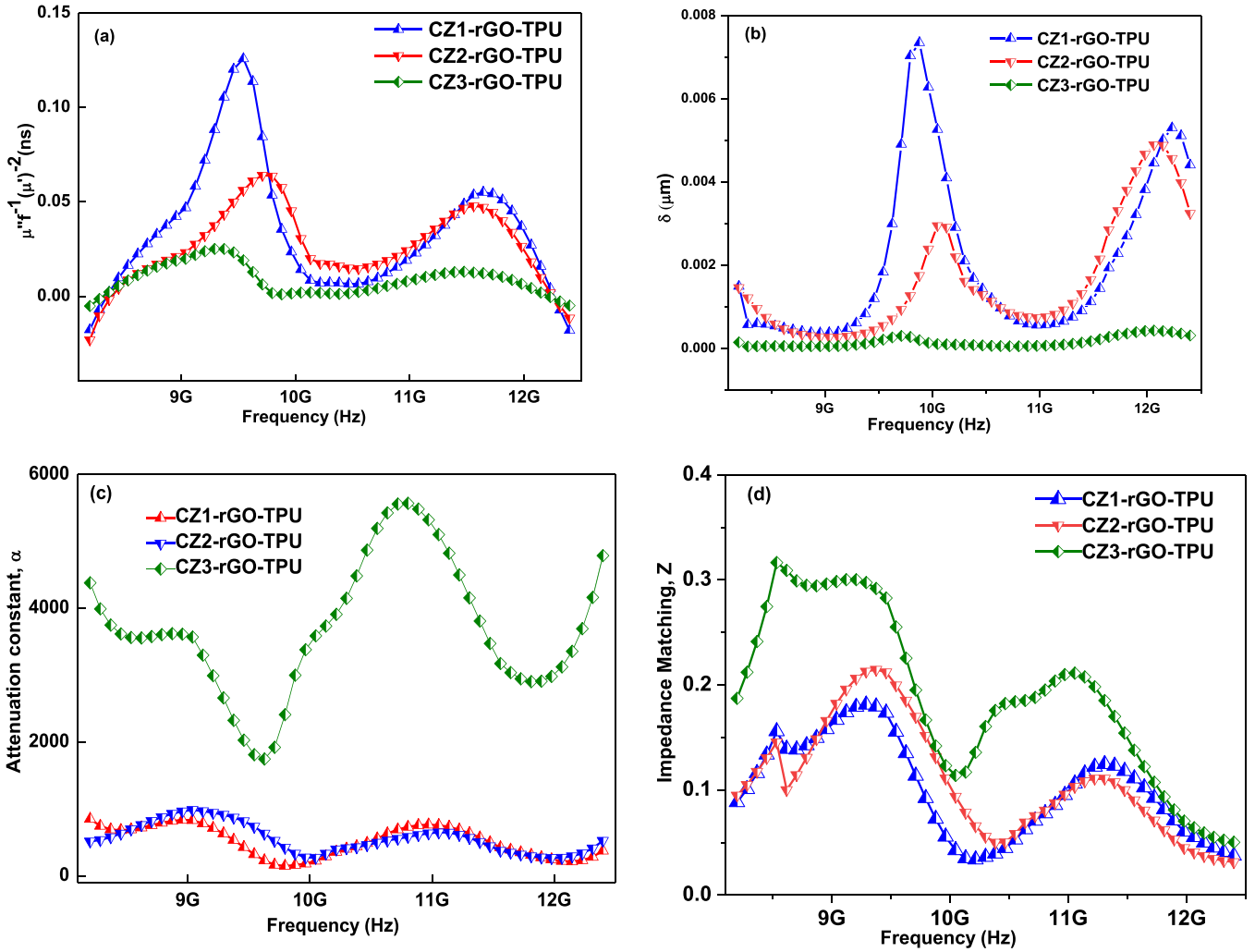

Figure 11. (a) Eddy current loss, (b) skin depth, (c) attenuation constant, and (d) impedance matching of CZ1-rGO-TPU, CZ2-rGO-TPU, and CZ3-rGO-TPU nanocomposites.

Further, the imaginary part (ε'') of the permittivity refers to the dissipation ability of electric energy. The imaginary part (ε'') of permittivity with the variation of frequency is shown in Figure 9b for the prepared nanocomposites CZ1-rGO-TPU, CZ2-rGO-TPU, and CZ3-rGO-TPU. The values of ε'' range from 0.07 to 0.36, 0.08 to 0.48, and 0.24 to 0.46 for CZ1-rGO-TPU, CZ2-rGO-TPU, and CZ3-rGO-TPU, respectively. Further, the pure TPU exhibits insulating behavior with electrical conductivity in the range of 10^{-12} S/cm.[94] The experimentally determined direct current (dc) conductivity is in the range of (1.6−3.8) × 10^{-10} S/cm for the prepared nanocomposites. An improvement in the electrical conductivity is noticed due to the presence of rGO in the TPU matrix. The influence of ferrite nanoparticles on dc conductivity is less, as these nanoparticles do not possess free electrons in the structures.[95] However, dielectric polarization can be induced under the applied EM field in such structures, which has a contribution to dielectric loss.[96,97]

In general, the Debye theory has been widely utilized to explain the relaxation mechanism in electromagnetic shielding materials. Based on the Debye theory, the relative complex permittivity has the following relation[98]

$$\varepsilon_r = \varepsilon_\infty + \frac{\varepsilon_s - \varepsilon_\infty}{1 + j\omega\tau} = \varepsilon' - j\varepsilon''$$

where ε_∞, ε_s, ω, and τ are the relative dielectric permittivity at an infinite frequency, the static dielectric permittivity, the angular frequency, and the polarization relaxation time, respectively. ε' and ε'' can be expressed as

$$\varepsilon' = \varepsilon_\infty + \frac{\varepsilon_s - \varepsilon_\infty}{1 + (\omega\tau)^2}$$

$$\varepsilon'' = \frac{\varepsilon_s - \varepsilon_\infty}{1 + (\omega\tau)^2}\omega\tau + \frac{\sigma}{\omega\varepsilon_o}$$

ε' and ε'' are mutually dependent on each other as they are dependent on $\omega\tau$. With the ignorance of the role of σ to ε'' and elimination of $\omega\tau$, the relation between ε' and ε'' can be expressed as

$$\left(\varepsilon' - \frac{\varepsilon_s + \varepsilon_\infty}{2}\right)^2 + (\varepsilon'')^2 = \left(\frac{\varepsilon_s - \varepsilon_\infty}{2}\right)^2$$

The above equation signifies that the plot of ε'' and ε' should be a semicircle, which is known as a Cole−Cole semicircle.[99] Figure 9c depicts the Cole−Cole plots for CZ1-rGO-TPU, CZ2-rGO-TPU, and CZ3-rGO-TPU nanocomposites. It can

https://doi.org/10.1021/acsomega.1c04192
ACS Omega 2021, 6, 28098−28118

be noticed that at least three Cole−Cole semicircles are present, which signifies the presence of multiple relaxation mechanisms in the prepared nanocomposites.[100]

The real part (μ') of permeability refers to the storage abilities of magnetic energy. μ' with a variation of frequency is in the range of 0.81−1.75, 1.06−2.13, and 2.05−3.15 for CZ1-rGO-TPU, CZ2-rGO-TPU, and CZ3-rGO-TPU, respectively (Figure 10a). Further, the imaginary part (μ'') of permeability signifies the dissipation ability of magnetic energy. With a variation of the frequency, the values of μ'' fluctuate in the ranges between −0.51 and 1.22, −0.44 and 1.08, and −0.49 and 1.49 for CZ1-rGO-TPU, CZ2-rGO-TPU, and CZ3-rGO-TPU, respectively (Figure 10b). In general, negative imaginary permeability is noticed in carbonaceous/magnetic composite materials.[101,102] The observed negative imaginary permeability is associated with the radiated magnetic energy intensively converted into electric energy. It leads to the transformation between the permittivity and permeability; consequently, the increase in the value of ε'', in turn, causes a decrease in the value of μ'' and becomes negative.[103]

Furthermore, for the comparative analysis of the dielectric loss abilities of the prepared nanocomposites, the dielectric loss tangents ($\tan\delta_\varepsilon = \varepsilon''/\varepsilon'$) is evaluated. The dielectric loss ($\tan\delta_\varepsilon$) of CZ1-rGO-TPU, CZ2-rGO-TPU, and CZ3-rGO-TPU nanocomposites is depicted in Figure 10c. The values of $\tan\delta_\varepsilon$ are in the range of 0.02−0.10, 0.02−0.13, and 0.05−0.09 for CZ1-rGO-TPU, CZ2-rGO-TPU, and CZ3-rGO-TPU, respectively. According to electromagnetic theory, dielectric loss is the contribution of intrinsic electromagnetic characteristics of the nanocomposites. The presence of polarization and associated relaxation is responsible for the dielectric loss in the developed nanocomposites.[104] The presence of residual groups and defects in rGO plays a role in the absorption of electromagnetic energy.

Also, for the comparative analysis of the magnetic loss capabilities of the developed nanocomposites, the magnetic loss tangents ($\tan\delta_\mu = \mu''/\mu'$) is assessed. The values of $\tan\delta_\mu$ range from −0.28 to 1.06, −0.29 to 0.76, and −0.15 to 0.56 for CZ1-rGO-TPU, CZ2-RGO-TPU, and CZ3-RGO-TPU, respectively (Figure 10d).

Generally, the magnetic loss of the shielding material is associated with natural resonance and eddy currents.[105] The impact of eddy currents on the magnetic loss can be evaluated by the following relation

$$C_o = \mu''(\mu')^{-2} f^{-1}$$

If the frequency dependent C_o value is constant, the eddy current is responsible for the magnetic loss in the shielding material. Figure 11a depicts the frequency dependence variation of C_o for the developed TPU-based nanocomposites. It can be noticed that the C_o value is almost constant over the frequency range of 10.13−10.64, 10.17−10.80, and 9.86−10.96 GHz for CZ1-rGO-TPU, CZ2-rGO-TPU, and CZ3-rGO-TPU, respectively. It indicates that the eddy current effect is the main contributor to the magnetic loss in this frequency range. Beyond this frequency range, natural resonance may be the main contributor to the magnetic loss for these nanocomposites.[106] The natural resonance can be expressed by the following relation[107]

$$2\pi f_r = \gamma H_a$$

where γ is the gyromagnetic ratio and H_a is the anisotropy energy. It is well known that the improvement in anisotropy energy (H_a) helps to enhance the electromagnetic wave absorption properties.[108] From the equation mentioned in Section 2.6 (magnetic properties), H_a increases as M_s decreases. Further, the anisotropy energy (H_a) of nanosized materials would be remarkably increased because of the surface anisotropy field effect.[109] Hence, H_a can be influenced not only by the particle size but also by the saturation magnetization.

The skin depth (δ), which is the distance for the electromagnetic wave to be attenuated to $1/e$ (37%) of its incident wave, can be expressed as[110]

$$\delta = \frac{1}{\sqrt{\pi\mu\sigma f}}$$

where μ and σ are the magnetic permeability and electrical conductivity, respectively, of the shielding material. Figure 11b shows the skin depths (δ) of CZ1-rGO-TPU, CZ2-rGO-TPU, and CZ3-rGO-TPU nanocomposites. The values of skin depths range from 0.0005 to 0.007, 0.0002 to 0.004, and 0.0003 to 0.0004 μm for CZ1-rGO-TPU, CZ2-rGO-TPU, and CZ3-rGO-TPU, respectively.

In general, the attenuation constant (α) can provide the electromagnetic wave attenuation capacity of the shielding material.[111] The attenuation constant can be evaluated by utilizing the following relation[112]

$$\alpha = \frac{\sqrt{2}\pi f}{c}\sqrt{(\mu''\varepsilon'' - \mu'\varepsilon') + \sqrt{(\mu''\varepsilon'' - \mu'\varepsilon')^2 + (\varepsilon'\mu'' + \varepsilon''\mu')^2}}$$

where c is the velocity of light and f is the frequency of the electromagnetic wave. The frequency-dependent attenuation constant (α) of nanocomposites is depicted in Figure 11c. It can be noticed that the CZ3-rGO-TPU nanocomposite has a higher α value in comparison with CZ1-rGO-TPU and CZ2-rGO-TPU nanocomposites. The value of the attenuation constant is not the only prerequisite for excellent electromagnetic shielding characteristics.[113] For the determination of the electromagnetic wave absorption by the shielding material, better impedance matching resulting from a balance between permeability and permittivity is also required.[114] In general, the electromagnetic wave absorption level of the shielding material is determined by impedance matching. The value of $Z = |Z_{in}/Z_o|$ can provide the degree of impedance matching. At $|Z_{in}/Z_o|$ equal to or close to 1, the shielding material can achieve full absorption or zero reflection, which signifies that the shielding material has high electromagnetic waves absorption.[115] The impedance matching (Z) value can be evaluated by utilizing the following relation[116]

$$Z = \left|\frac{Z_{in}}{Z_o}\right| = \sqrt{\mu_r/\varepsilon_r} = \sqrt{\sqrt{(\mu'^2 + \mu''^2)}/\sqrt{(\varepsilon'^2 + \varepsilon''^2)}}$$

Figure 11d depicts the frequency dependence of the impedance matching (Z) value of the prepared TPU-based nanocomposites. It can be noticed that the CZ3-rGO-TPU nanocomposite has a higher impedance matching value in comparison with the other prepared nanocomposites. The impedance matching was greatly enhanced in the CZ3-rGO-TPU nanocomposite in comparison with other developed nanocomposites.[117,118] The developed CZ3-rGO-TPU nanocomposite exhibits not only a high attenuation constant but also high impedance matching; consequently, it possesses excellent electromagnetic interference shielding characteristics.

https://doi.org/10.1021/acsomega.1c04192
ACS Omega 2021, 6, 28098−28118

Scheme 1. Schematic Illustration of the Electromagnetic Interference Shielding Mechanism in TPU-Matrix-Based Nanocomposites with Zn^{2+}-Substituted $CoFe_2O_4$ Spinel Ferrite Nanoparticles and rGO as Nanofillers

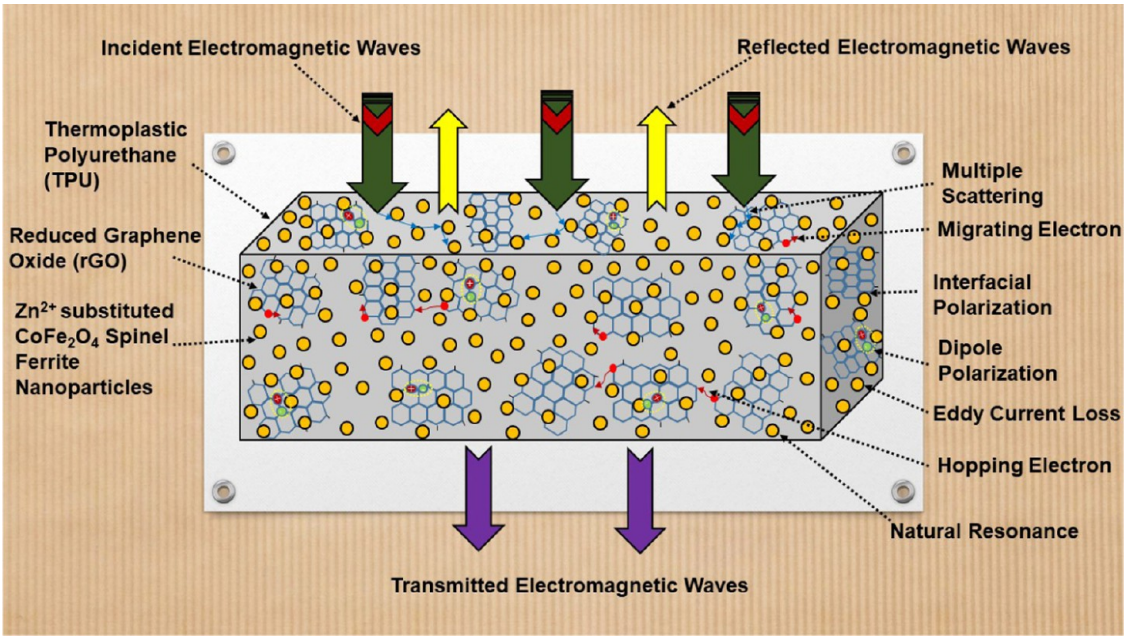

Therefore, the dipole and interfacial polarization, conduction loss, multiple scattering, eddy current effect, natural resonance, improved impedance matching, and attenuation constant result in the high-performance shielding effectiveness of the CZ3-rGO-TPU nanocomposite.

According to the above analysis and discussions, a possible electromagnetic interference shielding mechanism based on the prepared Zn^{2+}-substituted $CoFe_2O_4$ spinel ferrite nanoparticles-rGO-TPU nanocomposites has been proposed and illustrated in Scheme 1. The substitution of Zn^{2+} in the $CoFe_2O_4$ spinel ferrite nanoparticles affects both the magnetic and dielectric loss, which directly determines the electromagnetic interference shielding performance. Based on Debye theory, ε'' provides conduction loss and relaxation loss.[119] Under electromagnetic wave penetration in the prepared nanocomposites, the electrons migrate in the rGO nanosheets and hop between two neighboring rGO nanosheets or across the defects in rGO, as depicted in Scheme 1. It generates microcurrents, which increases the conduction loss. The relaxation loss associated with dipole polarization and interfacial polarization arises due to the functional groups, defects, and the interface between the spinel ferrite nanoparticles and rGO nanosheets or spinel ferrite nanoparticles interfaces or rGO nanosheets interfaces,[120] as depicted in Scheme 1. Further, the eddy current effect and natural resonance as magnetic losses are responsible for enhancing electromagnetic wave absorption.[121] Furthermore, with the substitution of Zn^{2+} in $CoFe_2O_4$ nanoparticles, magnetic characteristics change from ferromagnetic to superparamagnetism and consequently impact magnetic loss. The tailoring of the magnetic characteristics of $CoFe_2O_4$ nanoparticles by Zn^{2+} is beneficial to receive efficient synergy between magnetic loss and dielectric loss and to enhance impedance matching. In brief, better impedance matching, conduction loss, the synergistic effect of dielectric loss and magnetic loss, and multiple reflections and scattering can be responsible factors for high-performance EMI shielding characteristics of the TPU nanocomposite containing 20 wt % $Co_{0.33}Zn_{0.67}Fe_2O_4$ combined with reduced graphene oxide.

2.9. Mechanical Properties of Nanocomposites. Figure 12 depicts typical stress−strain curves of the prepared nanocomposites. The evaluated values of Young's modulus are 23 ± 3 and 18 ± 4 MPa for CZ1-rGO-TPU and CZ3-rGO-TPU, respectively. Abrisham et al.[122] noticed Young's modulus of 6.2−19.6 MPa for TPU composites with the carbon nanotubes and montmorillonite nanosheets. Bera et al.[123] observed Young's modulus of 2.2 MPa for TPU and 3.5−5.4 MPa for TPU/amine-functionalized GO nanocomposites. Further, the evaluated values of tensile strength are 3.1 ± 0.6 and 2.3 ± 0.3 MPa for CZ1-rGO-TPU and CZ3-rGO-TPU, respectively. In addition, the evaluated values of elongation at break are 72 and 43% for CZ1-rGO-TPU and CZ3-rGO-TPU, respectively. The observed mechanical characteristics imply

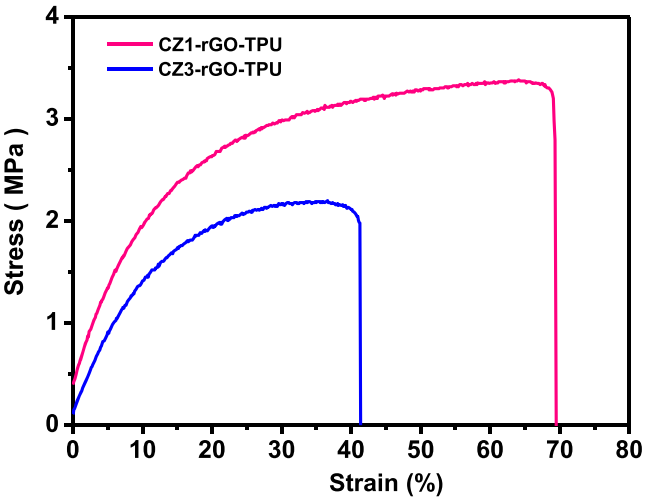

Figure 12. Representative stress−strain curves of CZ1-rGO-TPU and CZ3-rGO-TPU nanocomposites.

https://doi.org/10.1021/acsomega.1c04192
ACS Omega 2021, 6, 28098−28118

Scheme 2. Schematic Illustration of the Preparation of Spinel Ferrite Nanoparticles by the Sonochemical Method

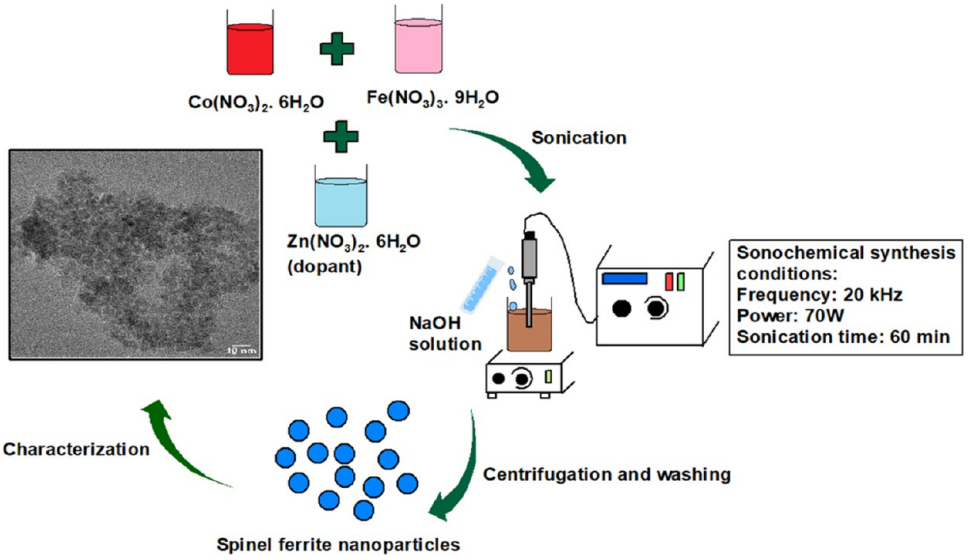

that the size of the prepared spinel ferrite nanoparticles influences the mechanical performance of the developed nanocomposites.[124] Menon et al.[125] noticed tensile strengths of 4.1−7.3 MPa and 56.2% recovery of tensile strength for the dopamine functionalized polyurethane (PU-Dopa)-Fe/MWNT composite.

3. CONCLUSIONS

In this work, we fabricated high-performance, lightweight, and flexible TPU-based nanocomposites with Zn^{2+}-substituted $CoFe_2O_4$ spinel ferrite nanoparticles (CZ1, CZ2, and CZ3) and rGO as nanofillers for EMI shielding application. The maximum total shielding effectiveness (SE_T) values in the frequency range of 8.2−12.4 GHz of the nanocomposites with a very low thickness of 0.8 mm were 48.3 dB, 61.8 dB, and 67.8 dB for CZ1-rGO-TPU, CZ2-rGO-TPU, and CZ3-rGO-TPU, respectively. The evaluated value of the specific shielding effectiveness (SSE) for the CZ3-rGO-TPU nanocomposite was 58 dB cm^3/g. The calculated value of absolute shielding effectiveness (SSE_t) of CZ3-rGO-TPU was 730 dB cm^2/g. The shielding efficiency of the CZ3-rGO-TPU nanocomposite was up to 99.9999%. The CZ3-rGO-TPU nanocomposite has a better balance between the dielectric and magnetic loss to reach the improved impedance matching condition, which results in high electromagnetic interference shielding performance. The prepared lightweight and flexible nanocomposite is an ideal candidate for practical applications in aircraft, satellite, telecommunications, and in the field of radar stealth.

4. EXPERIMENTAL SECTION

4.1. Chemicals. Cobalt nitrate hexahydrate, ferric nitrate nonahydrate, zinc nitrate hexahydrate, and sodium hydroxide were procured from Alfa Aesar GmbH and Co KG, Germany. Graphite flakes and potassium permanganate were obtained from Sigma-Aldrich, Germany. Sodium nitrate was acquired from Lach-Ner, Czech Republic. Vitamin C (Livsane), which was utilized as a reducing agent, was a product from Dr. Kleine Pharma GmbH, Germany.

4.2. Sonochemical Synthesis of Nanoparticles. In a typical synthesis, an aqueous solution of the stoichiometric amount of cobalt nitrate/zinc nitrate and iron nitrate was reacted with NaOH aqueous solution under the influence of sonication waves. Sonication was done for 1 h using an ultrasonic homogenizer UZ SONOPULS HD 2070. After the precipitate was formed due to the reaction between the nitrate solutions and sodium hydroxide under sonication, the sonication was stopped, and the formed precipitate was removed and washed with plenty of deionized water and ethanol. Then, the obtained product was dried in an oven at 60 °C for 24 h. The prepared nanoparticles of various compositions such as $CoFe_2O_4$, $Co_{0.67}Zn_{0.33}Fe_2O_4$, and $Co_{0.33}Zn_{0.67}Fe_2O_4$ were labeled CZ1, CZ2, and CZ3, respectively. A schematic of the preparation of these spinel ferrite nanoparticles is shown in Scheme 2.

4.3. Preparation of Reduced Graphene Oxide (rGO). Based on the Hummers method,[126] graphene oxide was synthesized by oxidizing expandable graphite flakes in our laboratory. In a typical synthesis, graphite flakes (3 g) and sodium nitrate (1.5 g) were dispersed in concentrated sulfuric acid (75 mL). Further, potassium permanganate (9 g) was added gradually to the above-prepared solution and kept at room temperature for 12 h. H_2O_2 (30%, 2 mL) was utilized for further treatment of the above mixture solution. The obtained mixture was further washed with deionized water to eliminate the residual ions. The obtained product was annealed at 60 °C for 24 h. The achieved graphene oxide (GO) was further reduced to reduced graphene oxide (rGO) by vitamin C as a reducing agent according to our previous report.[127]

4.4. Preparation of Nanocomposites. A micro-compounder (MC5, Xplore Instruments BV, Sittard, The Netherlands) with a capacity of 5 cm^3 consisting of twin screws was utilized to prepare the nanocomposites. Thermoplastic polyurethane (TPU) (Elastollan C80A10), spinel ferrite nanoparticles, and reduced graphene oxide were added together through the hopper into the running micro-compounder. The melt mixing conditions were 200 °C for 7 min at 150 rpm. Before melt mixing, TPU and fillers were dried in a vacuum oven at 90 °C for 12 h. The TPU-based nanocomposites containing 20 wt % nanofillers (which consisted of spinel ferrite nanoparticles and rGO in a 9:1 wt % ratio) were studied. Three nanocomposite series, designated CZ1-rGO-TPU, CZ2-rGO-TPU, and CZ3-rGO-TPU, were

https://doi.org/10.1021/acsomega.1c04192
ACS Omega 2021, 6, 28098−28118

Scheme 3. Schematic Illustration of the Preparation of TPU-Based Nanocomposites with Spinel Ferrite Nanoparticles with Reduced Graphene Oxide

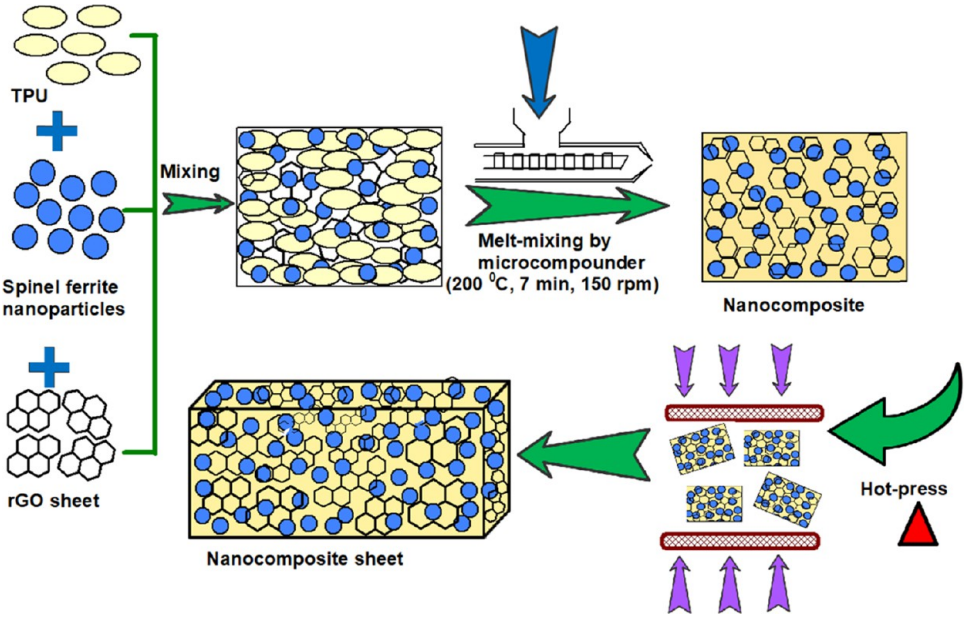

Figure 13. Digital photographs of the developed TPU-based nanocomposite with spinel ferrite nanoparticles and reduced graphene oxide demonstrating the dimension, lightweight, and flexibility.

developed. Further, the prepared TPU-based nanocomposites were compression-molded to form rectangular-shaped sheets with dimensions of 22.9 mm × 10.2 mm × 0.8 mm. A schematic illustration of the development of TPU nanocomposites containing spinel ferrite nanoparticles and reduced graphene oxide as nanofillers is shown in Scheme 3. Representative digital photographs of a developed CZ1-rGO-TPU nanocomposite are shown in Figure 13.

4.5. Characterization Techniques. FTIR spectra of the prepared nanoparticles and their TPU-based nanocomposites were obtained using the FTIR spectrometer (Nicolet 6700) (Thermo Scientific, Waltham, MA) in attenuated total reflectance mode. Raman spectroscopic measurements were obtained with a Raman microscope Nicolet DXR (Thermo Fisher Scientific, Waltham, MA) at laser excitation wavelengths of 532 and 780 nm. XPS spectra were obtained with an X-ray photoelectron spectroscope using Kratos Analytical Axis Ultra DLD system. XRD patterns were studied with an X-ray diffractometer using Rigaku MiniFlex 600 (Rigaku Corporation, Tokyo, Japan). The morphology of the prepared nanoparticles was investigated by transmission electron microscopy (TEM) and high-resolution TEM (HRTEM) using a JEM-2100Plus (Jeol, Tokyo, Japan) as well as by field emission scanning electron microscopy (FE-SEM) using an FEI NanoSEM450 (FEI Company, The Netherlands). The morphology of the composites was studied by FE-SEM on surfaces of cryofractures prepared from compression-molded sheets. The complex permittivity, complex permeability, and *S* parameters were measured on a PNA-L network analyzer (Agilent N5230A) using an X-band (WR 90) waveguide operating within the frequency range of 8.2−12.4 GHz. Rectangular specimens with dimensions of 22.9 mm × 10.2 mm × 0.8 mm matching the inner cross section of the waveguide were cut out from the prepared composite sheets and placed inside a waveguide section. The obtained *S* parameters were utilized to evaluate the total shielding effectiveness (SE_T), shielding effectiveness due to reflection (SE_R), and shielding effectiveness due to absorption (SE_A). The techniques of Nicolson−Ross−Weir are utilized, which provide a direct assessment of complex permittivity and permeability using input *S*-parameters. The dc conductivity was measured using the set for 2-points method, where the *I*−*V* characteristics were measured in the two-point setup using electrodes of cylindrical shape (d = 16 mm) with a programmable electrometer (Keithley 6517 A). Magnetic characteristics of samples were studied using a vibrating

https://doi.org/10.1021/acsomega.1c04192
ACS Omega 2021, 6, 28098−28118

sample magnetometer (VSM, Model 7404, Lake Shore, Westerville, OH). Thermogravimetric analysis (TGA) was performed using a Setaram LabSys Evo with the TG/DSC sensor in an atmosphere of air. Mechanical characteristics of TPU nanocomposites were studied by utilizing a Testometric universal-testing machine of type M 350−5CT (Testometric Co. Ltd., Rochdale, UK).

■ ASSOCIATED CONTENT

Supporting Information

The Supporting Information is available free of charge at https://pubs.acs.org/doi/10.1021/acsomega.1c04192.

XPS study of spinel ferrite nanoparticles (Figure S1), GO, and rGO (Figure S2); some additional FE-SEM images of the fractured surfaces of CZ3-RGO-TPU nanocomposites (Figure S3a,b, the portion of the SEM image, which was utilized for the EDX study (Figure S3c); the elemental mapping images of the CZ2-rGO-TPU nanocomposite (Figure S4); the interplanar spacing *d* (nm) values indexed using Miller indices (*hkl* planes) for the prepared nanoparticles (Table S1); and TGA of TPU and prepared nanocomposites (Figure S5) (PDF)

■ AUTHOR INFORMATION

Corresponding Author

Raghvendra Singh Yadav − *Centre of Polymer Systems, University Institute, Tomas Bata University in Zlín, 760 01 Zlín, Czech Republic;* orcid.org/0000-0003-1773-3596; Phone: +420-576031725; Email: yadav@utb.cz

Authors

Anju − *Centre of Polymer Systems, University Institute, Tomas Bata University in Zlín, 760 01 Zlín, Czech Republic*

Petra Pötschke − *Leibniz Institute of Polymer Research Dresden (IPF Dresden), 01069 Dresden, Germany;* orcid.org/0000-0001-6392-7880

Jürgen Pionteck − *Leibniz Institute of Polymer Research Dresden (IPF Dresden), 01069 Dresden, Germany;* orcid.org/0000-0003-2310-1106

Beate Krause − *Leibniz Institute of Polymer Research Dresden (IPF Dresden), 01069 Dresden, Germany*

Ivo Kuřitka − *Centre of Polymer Systems, University Institute, Tomas Bata University in Zlín, 760 01 Zlín, Czech Republic;* orcid.org/0000-0002-1016-5170

Jarmila Vilcakova − *Centre of Polymer Systems, University Institute, Tomas Bata University in Zlín, 760 01 Zlín, Czech Republic*

David Skoda − *Centre of Polymer Systems, University Institute, Tomas Bata University in Zlín, 760 01 Zlín, Czech Republic;* orcid.org/0000-0002-3787-1956

Pavel Urbánek − *Centre of Polymer Systems, University Institute, Tomas Bata University in Zlín, 760 01 Zlín, Czech Republic*

Michal Machovsky − *Centre of Polymer Systems, University Institute, Tomas Bata University in Zlín, 760 01 Zlín, Czech Republic*

Milan Masař − *Centre of Polymer Systems, University Institute, Tomas Bata University in Zlín, 760 01 Zlín, Czech Republic*

Michal Urbánek − *Centre of Polymer Systems, University Institute, Tomas Bata University in Zlín, 760 01 Zlín, Czech Republic*

Marek Jurca − *Centre of Polymer Systems, University Institute, Tomas Bata University in Zlín, 760 01 Zlín, Czech Republic*

Lukas Kalina − *Materials Research Centre, Brno University of Technology, 61200 Brno, Czech Republic*

Jaromir Havlica − *Materials Research Centre, Brno University of Technology, 61200 Brno, Czech Republic*

Complete contact information is available at: https://pubs.acs.org/10.1021/acsomega.1c04192

Notes

The authors declare no competing financial interest.

■ ACKNOWLEDGMENTS

The authors acknowledge the financial support of the Czech Science Foundation (GA19-23647S) project at the Centre of Polymer Systems, Tomas Bata University in Zlin, Czech Republic. R.S.Y. thanks the Leibniz Institute of Polymer Research Dresden, Germany, for hosting as Guest Scientist in its laboratories.

■ REFERENCES

(1) Yadav, R. S.; Kuritka, I.; Vilcakova, J. *Advanced Spinel Ferrite Nanocomposites for Electromagnetic Interference Shielding Applications*, 1st ed.; Elsevier Publishing, 2020.

(2) Huang, Y.; Wang, Y.; Li, Z.; Yang, Z.; Shen, C.; He, C. Effect of Pore Morphology on the Dielectric Properties of Porous Carbons for Microwave Absorption Applications. *J. Phys. Chem. C* **2014**, *118*, 26027−26032.

(3) Rehman, S. U.; Liu, J.; Fang, Z.; Wang, J.; Ahmed, R.; Wang, C.; Bi, H. Heterostructured TiO_2/C/Co from ZIF-67 Frameworks for Microwave-Absorbing Nanomaterials. *ACS Appl. Nano Mater.* **2019**, *2*, 4451−4461.

(4) Jian, X.; Xiao, X.; Deng, L.; Tian, W.; Wang, X.; Mahmood, N.; Dou, S. Heterostructured Nanorings of Fe−Fe_3O_4@C Hybrid with Enhanced Microwave Absorption Performance. *ACS Appl. Mater. Interfaces* **2018**, *10*, 9369−9378.

(5) Guan, G.; Gao, G.; Xiang, J.; Yang, J.; Gong, L.; Chen, X.; Zhang, Y.; Zhang, K.; Meng, X. $CoFe_2$/$BaTiO_3$ Hybrid Nanofibers for Microwave Absorption. *ACS Appl. Nano Mater.* **2020**, *3*, 8424−8437.

(6) Li, Y.; Gao, T.; Zhang, W.; Hu, H.; Rong, H.; Zhang, X. Fe@CNx Nanocapsules for Microwave Absorption at Gigahertz Frequency. *ACS Appl. Nano Mater.* **2019**, *2*, 3648−3653.

(7) Bora, P. J.; Azeem, I.; Vinoy, K. J.; Ramamurthy, P. C.; Madras, G. Polyvinylbutyral−Polyaniline Nanocomposite for High Microwave Absorption Efficiency. *ACS Omega* **2018**, *3*, 16542−16548.

(8) Yadav, R. S.; Anju; Jamatia, T.; Kuřitka, I.; Vilčáková, J.; Škoda, D.; Urbánek, P.; Machovský, M.; Masař, M.; Urbánek, M.; et al. Excellent, Lightweight and Flexible Electromagnetic Interference Shielding Nanocomposites Based on Polypropylene with $MnFe_2O_4$ Spinel Ferrite Nanoparticles and Reduced Graphene Oxide. *Nanomaterials* **2020**, *10*, No. 2481.

(9) Chen, Y.; Pötschke, P.; Pionteck, J.; Voit, B.; Qi, H. Multifunctional Cellulose/rGO/Fe_3O_4 Composite Aerogels for Electromagnetic Interference Shielding. *ACS Appl. Mater. Interfaces* **2020**, *12*, 22088−22098.

(10) Han, G.; Ma, Z.; Zhou, B.; He, C.; Wang, B.; Feng, Y.; Ma, J.; Sun, L.; Liu, C. Cellulose-Based Ni-Decorated Graphene Magnetic Film for Electromagnetic Interference Shielding. *J. Colloid Interface Sci.* **2021**, *583*, 571−578.

(11) Acharya, S.; Datar, S. Wideband (8−18 GHz) Microwave Absorption Dominated Electromagnetic Interference (EMI) Shielding Composite Using Copper Aluminum Ferrite and Reduced Graphene Oxide in Polymer Matrix. *J. Appl. Phys.* **2020**, *128*, No. 104902.

(12) Fei, Y.; Liang, M.; Yan, L.; Chen, Y.; Zou, H. Co/C@cellulose Nanofiber Aerogel Derived from Metal-Organic Frameworks for

Highly Efficient Electromagnetic Interference Shielding. *Chem. Eng. J.* **2020**, *392*, No. 124815.
(13) Shin, B.; Mondal, S.; Lee, M.; Kim, S.; Huh, Y.-I.; Nah, C. Flexible thermoplastic polyurethane-carbon nanotube composites for electromagnetic interference shielding and thermal management. *Chem. Eng. J.* **2021**, *418*, No. 129282.
(14) Huang, S.-C.; Deng, C.; Chen, H.; Li, Y.-M.; Zhao, Z.-Y.; Wang, S.-X.; Wang, Y.-Z. Novel Ultrathin Layered Double Hydroxide Nanosheets with In Situ Formed Oxidized Phosphorus as Anions for Simultaneous Fire Resistance and Mechanical Enhancement of Thermoplastic Polyurethane. *ACS Appl. Polym. Mater.* **2019**, *1*, 1979−1990.
(15) Danda, C.; Amurin, L. G.; Muñoz, P. A. R.; Nagaoka, D. A.; Schneider, T.; Troxell, B.; Khani, S.; Domingues, S. H.; Andrade, R. J. E.; Fechine, G. J. M.; et al. Integrated Computational and Experimental Design of Ductile, Abrasion-Resistant Thermoplastic Polyurethane/Graphene Oxide Nanocomposites. *ACS Appl. Nano Mater.* **2020**, *3*, 9694−9705.
(16) Bhattacharjee, Y.; Biswas, S.; Bose, S. Thermoplastic Polymer Composites for EMI Shielding Applications. In *Materials for Potential EMI Shielding Applications*; Joseph, K.; Wilson, R.; George, G., Eds.; Elsevier, 2020; Chapter 5, pp 73−99. ISBN 978-0-12-817590-3.
(17) Sang, G.; Dong, J.; He, X.; Jiang, J.; Li, J.; Xu, P.; Ding, Y. Electromagnetic Interference Shielding Performance of Polyurethane Composites: A Comparative Study of GNs-IL/Fe_3O_4 and MWCNTs-IL/Fe_3O_4 Hybrid Fillers. *Composites, Part B* **2019**, *164*, 467−475.
(18) Valentini, M.; Piana, F.; Pionteck, J.; Lamastra, F. R.; Nanni, F. Electromagnetic Properties and Performance of Exfoliated Graphite (EG)—Thermoplastic Polyurethane (TPU) Nanocomposites at Microwaves. *Compos. Sci. Technol.* **2015**, *114*, 26−33.
(19) Jun, Y.; Habibpour, S.; Hamidinejad, M.; Park, M. G.; Ahn, W.; Yu, A.; Park, C. B. Enhanced Electrical and Mechanical Properties of Graphene Nano-Ribbon/Thermoplastic Polyurethane Composites. *Carbon* **2021**, *174*, 305−316.
(20) Shen, B.; Li, Y.; Zhai, W.; Zheng, W. Compressible Graphene-Coated Polymer Foams with Ultralow Density for Adjustable Electromagnetic Interference (EMI) Shielding. *ACS Appl. Mater. Interfaces* **2016**, *8*, 8050−8057.
(21) Hsiao, S.-T.; Ma, C.-C. M.; Tien, H.-W.; Liao, W.-H.; Wang, Y.-S.; Li, S.-M.; Yang, C.-Y.; Lin, S.-C.; Yang, R.-B. Effect of Covalent Modification of Graphene Nanosheets on the Electrical Property and Electromagnetic Interference Shielding Performance of a Water-Borne Polyurethane Composite. *ACS Appl. Mater. Interfaces* **2015**, *7*, 2817−2826.
(22) Jia, L.-C.; Yan, D.-X.; Liu, X.; Ma, R.; Wu, H.-Y.; Li, Z.-M. Highly Efficient and Reliable Transparent Electromagnetic Interference Shielding Film. *ACS Appl. Mater. Interfaces* **2018**, *10*, 11941−11949.
(23) Menon, A. V.; Madras, G.; Bose, S. Ultrafast Self-Healable Interfaces in Polyurethane Nanocomposites Designed Using Diels−Alder "Click" as an Efficient Microwave Absorber. *ACS Omega* **2018**, *3*, 1137−1146.
(24) Zahid, M.; Nawab, Y.; Gulzar, N.; Rehan, Z. A.; Shakir, M. F.; Afzal, A.; Abdul Rashid, I.; Tariq, A. Fabrication of Reduced Graphene Oxide (RGO) and Nanocomposite with Thermoplastic Polyurethane (TPU) for EMI Shielding Application. *J. Mater. Sci.: Mater. Electron.* **2020**, *31*, 967−974.
(25) Liu, T.; Pang, Y.; Kikuchi, H.; Kamada, Y.; Takahashi, S. Superparamagnetic property and high microwave absorption performance of FeAl@$(Al, Fe)_2O_3$ nanoparticles induced by surface oxidation. *J. Mater. Chem. C* **2015**, *3*, 6232−6239.
(26) Ramesh, G. V.; Sudheendran, K.; James Raju, K. C.; Sreedhar, B.; Radhakrishnan, T. P. Microwave Absorber Based on Silver Nanoparticle-Embedded Polymer Thin Film. *J. Nanosci. Nanotechnol.* **2009**, *9*, 261−266.
(27) Kong, I. *Design and Applications of Nanostructured Polymer Blends and Nanocomposite Systems*; Elsevier, 2016; Chapter 7, pp 125−154.
(28) Kolev, S.; Yanev, A.; Nedkov, I. Microwave absorption of ferrite powders in a polymer matrix. *Phys. Status Solidi C* **2006**, *3*, 1308−1315.
(29) Yan, D.; Cheng, S.; Zhuo, R. F.; Chen, J. T.; Feng, J. J.; Feng, H. T.; Li, H. J.; Wu, Z. G.; Wang, J.; Yan, P. X. Nanoparticles and 3D Sponge-like Porous Networks of Manganese Oxides and Their Microwave Absorption Properties. *Nanotechnology* **2009**, *20*, No. 105706.
(30) Wang, X.; Pakdel, A.; Zhang, J.; Weng, Q.; Zhai, T.; Zhi, C.; Golberg, D.; Bando, Y. Large-Surface-Area BN Nanosheets and Their Utilization in Polymeric Composites with Improved Thermal and Dielectric Properties. *Nanoscale Res. Lett.* **2012**, *7*, No. 662.
(31) Ding, L.; Zhao, X.; Huang, Y.; Yan, J.; Li, T.; Liu, P. Ultra-broadband and covalently linked core−shell $CoFe_2O_4$@PPynanoparticles with reduced graphene oxide for microwave absorption. *J. Colloid Interface Sci.* **2021**, *595*, 168−177.
(32) Zhang, X.-J.; Wang, G.-S.; Cao, W.-Q.; Wei, Y.-Z.; Liang, J.-F.; Guo, L.; Cao, M.-S. Enhanced Microwave Absorption Property of Reduced Graphene Oxide (RGO)-$MnFe_2O_4$ Nanocomposites and Polyvinylidene Fluoride. *ACS Appl. Mater. Interfaces* **2014**, *6*, 7471−7478.
(33) Yuan, H.; Xu, Y.; Jiaa, H.; Zhou, S. Superparamagnetic Fe_3O_4/MWCNTs heterostructures for high frequency microwave absorption. *RSC Adv.* **2016**, *6*, 67218−67225.
(34) He, J.; Liu, S.; Deng, L.; Shan, D.; Cao, C.; Luo, H.; Yan, S. Tunable Electromagnetic and Enhanced Microwave Absorption Properties in $CoFe_2O_4$ Decorated Ti_3C_2 MXene Composites. *Appl. Surf. Sci.* **2020**, *504*, No. 144210.
(35) Che, R. C.; Zhi, C. Y.; Liang, C. Y.; Zhou, X. G. Fabrication and Microwave Absorption of Carbon Nanotubes/$CoFe_2O_4$ Spinel Nanocomposite. *Appl. Phys. Lett.* **2006**, *88*, No. 033105.
(36) Houbi, A.; Aldashevich, Z. A.; Atassi, Y.; Bagasharova Telmanovna, Z.; Saule, M.; Kubanych, K. Microwave Absorbing Properties of Ferrites and Their Composites: A Review. *J. Magn. Magn. Mater.* **2021**, *529*, No. 167839.
(37) Kadam, R. H.; Borade, R. B.; Mane, M. L.; Mane, D. R.; Batoo, K. M.; Shirsath, S. E. Structural, Mechanical, Dielectric Properties and Magnetic Interactions in Dy^{3+}-Substituted Co−Cu−Zn Nanoferrites. *RSC Adv.* **2020**, *10*, 27911−27922.
(38) Anu, K.; Hemalatha, J. Magnetic and Electrical Conductivity Studies of Zinc Doped Cobalt Ferrite Nanofluids. *J. Mol. Liq.* **2019**, *284*, 445−453.
(39) Dippong, T.; Levei, E. A.; Deac, I. G.; Neag, E.; Cadar, O. Influence of Cu^{2+}, Ni^{2+}, and Zn^{2+} Ions Doping on the Structure, Morphology, and Magnetic Properties of Co-Ferrite Embedded in SiO_2 Matrix Obtained by an Innovative Sol-Gel Route. *Nanomaterials* **2020**, *10*, No. 580.
(40) Barick, A. K.; Tripathy, D. K. Preparation, Characterization and Properties of Acid Functionalized Multi-Walled Carbon Nanotube Reinforced Thermoplastic Polyurethane Nanocomposites. *Mater. Sci. Eng., B* **2011**, *176*, 1435−1447.
(41) Gao, J.; Hu, M.; Dong, Y.; Li, R. K. Y. Graphite-Nanoplatelet-Decorated Polymer Nanofiber with Improved Thermal, Electrical, and Mechanical Properties. *ACS Appl. Mater. Interfaces* **2013**, *5*, 7758−7764.
(42) Quickel, T. E.; Le, V. H.; Brezesinski, T.; Tolbert, S. H. On the Correlation between Nanoscale Structure and Magnetic Properties in Ordered Mesoporous Cobalt Ferrite ($CoFe_2O_4$) Thin Films. *Nano Lett.* **2010**, *10*, 2982−2988.
(43) Ortiz-Quiñonez, J.-L.; Pal, U.; Villanueva, M. S. Structural, Magnetic, and Catalytic Evaluation of Spinel Co, Ni, and Co−Ni Ferrite Nanoparticles Fabricated by Low-Temperature Solution Combustion Process. *ACS Omega* **2018**, *3*, 14986−15001.
(44) Wang, P.; Liu, Z.-G.; Chen, X.; Meng, F.-L.; Liu, J.-H.; Huang, X.-J. UV Irradiation Synthesis of an Au−Graphene Nanocomposite with Enhanced Electrochemical Sensing Properties. *J. Mater. Chem. A* **2013**, *1*, 9189−9195.

https://doi.org/10.1021/acsomega.1c04192
ACS Omega 2021, 6, 28098−28118

(45) Yin, F.; Wu, S.; Wang, Y.; Wu, L.; Yuan, P.; Wang, X. Self-Assembly of Mildly Reduced Graphene Oxide Monolayer for Enhanced Raman Scattering. *J. Solid State Chem.* **2016**, *237*, 57−63.
(46) Wu, N.; She, X.; Yang, D.; Wu, X.; Su, F.; Chen, Y. Synthesis of Network Reduced Graphene Oxide in Polystyrene Matrix by a Two-Step Reduction Method for Superior Conductivity of the Composite. *J. Mater. Chem.* **2012**, *22*, 17254−17261.
(47) Siong, V. L. E.; Lee, K. M.; Juan, J. C.; Lai, C. W.; Tai, X. H.; Khe, C. S. Removal of Methylene Blue Dye by Solvothermally Reduced Graphene Oxide: A Metal-Free Adsorption and Photodegradation Method. *RSC Adv.* **2019**, *9*, 37686−37695.
(48) Liu, H.; Dong, M.; Huang, W.; Gao, J.; Dai, K.; Guo, J.; Zheng, G.; Liu, C.; Shen, C.; Guo, Z. Lightweight Conductive Graphene/Thermoplastic Polyurethane Foams with Ultrahigh Compressibility for Piezoresistive Sensing. *J. Mater. Chem. C* **2017**, *5*, 73−83.
(49) Jing, X.; Mi, H.-Y.; Salick, M. R.; Cordie, T. M.; Peng, X.-F.; Turng, L.-S. Electrospinning Thermoplastic Polyurethane/Graphene Oxide Scaffolds for Small Diameter Vascular Graft Applications. *Mater. Sci. Eng., C* **2015**, *49*, 40−50.
(50) Nikmanesh, H.; Kameli, P.; Asgarian, S. M.; Karimi, S.; Moradi, M.; Kargar, Z.; Ventura, J.; Bordalo, B.; Salamati, H. Positron Annihilation Lifetime, Cation Distribution and Magnetic Features of $Ni_{1-x}Zn_xFe_{2-x}Co_xO_4$ Ferrite Nanoparticles. *RSC Adv.* **2017**, *7*, 22320−22328.
(51) Kumar, P.; Pathak, S.; Singh, A.; Khanduri, H.; Basheed, G. A.; Wang, L.; Pant, R. P. Microwave Spin Resonance Investigation on the Effect of the Post-Processing Annealing of $CoFe_2O_4$ Nanoparticles. *Nanoscale Adv.* **2020**, *2*, 1939−1948.
(52) Jangam, K.; Patil, K.; Balgude, S.; Patange, S.; More, P. Magnetically Separable $Zn_{1-x}Co_{0.5x}Mg_{0.5x}Fe_2O_4$ Ferrites: Stable and Efficient Sunlight-Driven Photocatalyst for Environmental Remediation. *RSC Adv.* **2020**, *10*, 42766−42776.
(53) Tong, W.; Zhang, Y.; Yu, L.; Luan, X.; An, Q.; Zhang, Q.; Lv, F.; Chu, P. K.; Shen, B.; Zhang, Z. Novel Method for the Fabrication of Flexible Film with Oriented Arrays of Graphene in Poly(Vinylidene Fluoride-Co-Hexafluoropropylene) with Low Dielectric Loss. *J. Phys. Chem. C* **2014**, *118*, 10567−10573.
(54) Zhang, W.; Zhang, Y.; Tian, Y.; Yang, Z.; Xiao, Q.; Guo, X.; Jing, L.; Zhao, Y.; Yan, Y.; Feng, J.; et al. Insight into the Capacitive Properties of Reduced Graphene Oxide. *ACS Appl. Mater. Interfaces* **2014**, *6*, 2248−2254.
(55) Rashti, A.; Wang, B.; Hassani, E.; Feyzbar-Khalkhali-Nejad, F.; Zhang, X.; Oh, T.-S. Electrophoretic Deposition of Nickel Cobaltite/Polyaniline/RGO Composite Electrode for High-Performance All-Solid-State Asymmetric Supercapacitors. *Energy Fuels* **2020**, *34*, 6448−6461.
(56) Xiang, C.; Cox, P. J.; Kukovecz, A.; Genorio, B.; Hashim, D. P.; Yan, Z.; Peng, Z.; Hwang, C.-C.; Ruan, G.; Samuel, E. L. G.; et al. Functionalized Low Defect Graphene Nanoribbons and Polyurethane Composite Film for Improved Gas Barrier and Mechanical Performances. *ACS Nano* **2013**, *7*, 10380−10386.
(57) Bera, M.; Prabhakar, A.; Maji, P. K. Nanotailoring of Thermoplastic Polyurethane by Amine Functionalized Graphene Oxide: Effect of Different Amine Modifier on Final Properties. *Composites, Part B* **2020**, *195*, No. 108075.
(58) Zhang, T.; Yang, J.; Zhang, N.; Huang, T.; Wang, Y. Achieving Large Dielectric Property Improvement in Poly(Ethylene Vinyl Acetate)/Thermoplastic Polyurethane/Multiwall Carbon Nanotube Nanocomposites by Tailoring Phase Morphology. *Ind. Eng. Chem. Res.* **2017**, *56*, 3607−3617.
(59) Sharifi Dehsari, H.; Asadi, K. Impact of Stoichiometry and Size on the Magnetic Properties of Cobalt Ferrite Nanoparticles. *J. Phys. Chem. C* **2018**, *122*, 29106−29121.
(60) Khan, M. A. M.; Khan, W.; Ahamed, M.; Ahmed, J.; Al-Gawati, M. A.; Alhazaa, A. N. Silver-Decorated Cobalt Ferrite Nanoparticles Anchored onto the Graphene Sheets as Electrode Materials for Electrochemical and Photocatalytic Applications. *ACS Omega* **2020**, *5*, 31076−31084.
(61) Yadav, R. S.; Havlica, J.; Hnatko, M.; Šajgalík, P.; Alexander, C.; Palou, M.; Bartoníčková, E.; Boháč, M.; Frajkorová, F.; Masilko, J.; et al. Magnetic Properties of $Co_{1-x}Zn_xFe_2O_4$ Spinel Ferrite Nanoparticles Synthesized by Starch-Assisted Sol−Gel Autocombustion Method and Its Ball Milling. *J. Magn. Magn. Mater.* **2015**, *378*, 190−199.
(62) Wang, X.; Zhu, T.; Chang, S.; Lu, Y.; Mi, W.; Wang, W. 3D Nest-Like Architecture of Core−Shell $CoFe_2O_4$@1T/2H-MoS_2 Composites with Tunable Microwave Absorption Performance. *ACS Appl. Mater. Interfaces* **2020**, *12*, 11252−11264.
(63) Guo, P.; Cui, L.; Wang, Y.; Lv, M.; Wang, B.; Zhao, X. S. Facile Synthesis of $ZnFe_2O_4$ Nanoparticles with Tunable Magnetic and Sensing Properties. *Langmuir* **2013**, *29*, 8997−9003.
(64) Zhu, J.; Wei, S.; Haldolaarachchige, N.; Young, D. P.; Guo, Z. Electromagnetic Field Shielding Polyurethane Nanocomposites Reinforced with Core−Shell Fe−Silica Nanoparticles. *J. Phys. Chem. C* **2011**, *115*, 15304−15310.
(65) Liu, X. G.; Geng, D. Y.; Ma, S.; Meng, H.; Tong, M.; Kang, D. J.; Zhang, Z. D. Electromagnetic-Wave Absorption Properties of FeCo Nanocapsules and Coral-like Aggregates Self-Assembled by the Nanocapsules. *J. Appl. Phys.* **2008**, *104*, No. 064319.
(66) Almessiere, M. A.; Slimani, Y.; Güngüneş, H.; Korkmaz, A. D.; Zubar, T.; Trukhanov, S.; Trukhanov, A.; Manikandan, A.; Alahmari, F.; Baykal, A. Influence of Dy3+ Ions on the Microstructures and Magnetic, Electrical, and Microwave Properties of $[Ni_{0.4}Cu_{0.2}Zn_{0.4}]$-$(Fe_{2-x}Dy_x)O4$ ($0.00 \leq x \leq 0.04$) Spinel Ferrites. *ACS Omega* **2021**, *6*, 10266−10280.
(67) Rondinone, A. J.; Samia, A. C. S.; Zhang, Z. J. Characterizing the Magnetic Anisotropy Constant of Spinel Cobalt Ferrite Nanoparticles. *Appl. Phys. Lett.* **2000**, *76*, 3624−3626.
(68) Manna, R.; Ghosh, K.; Srivastava, S. K. Functionalized Graphene/Nickel/Polyaniline Ternary Nanocomposites: Fabrication and Application as Electromagnetic Wave Absorbers. *Langmuir* **2021**, *37*, 7430−7441.
(69) Yin, X.; Kong, L.; Zhang, L.; Cheng, L.; Travitzky, N.; Greil, P. Electromagnetic Properties of Si−C−N Based Ceramics and Composites. *Int. Mater. Rev.* **2014**, *59*, 326−355.
(70) Cheng, Y.; Zhao, H.; Lv, H.; Shi, T.; Ji, G.; Hou, Y. Lightweight and Flexible Cotton Aerogel Composites for Electromagnetic Absorption and Shielding Applications. *Adv. Electron. Mater.* **2020**, *6*, No. 1900796.
(71) Verma, M.; Chauhan, S. S.; Dhawan, S. K.; Choudhary, V. Graphene nanoplatelets/carbon nanotubes/polyurethane composites as efficient shield against electromagnetic polluting radiations. *Composites, Part B* **2017**, *120*, 118−127.
(72) Shahzad, F.; Yu, S.; Kumar, P.; Lee, J.-W.; Kim, Y.-H.; Hong, S. M.; Koo, C. M. Sulfur doped graphene/polystyrene nanocomposites for electromagnetic interference shielding. *Compos. Struct.* **2015**, *133*, 1267−1275.
(73) Manna, K.; Srivastava, S. K. Contrasting Role of Defect-Induced Carbon Nanotubes in Electromagnetic Interference Shielding. *J. Phys. Chem. C* **2018**, *122*, 19913−19920.
(74) Shin, B.; Mondal, S.; Lee, M.; Kim, S.; Huh, Y.-I.; Nah, C. Flexible thermoplastic polyurethane-carbon nanotube composites for electromagnetic interference shielding and thermal management. *Chem. Eng. J.* **2021**, *418*, No. 129282.
(75) Li, L.; Cao, Y.; Liu, X.; Wang, J.; Yang, Y.; Wang, W. Multifunctional MXene-Based Fireproof Electromagnetic Shielding Films with Exceptional Anisotropic Heat Dissipation Capability and Joule Heating Performance. *ACS Appl. Mater. Interfaces* **2020**, *12*, 27350−27360.
(76) Liu, C.; Wang, X.; Huang, X.; Liao, X.; Shi, B. Absorption and Reflection Contributions to the High Performance of Electromagnetic Waves Shielding Materials Fabricated by Compositing Leather Matrix with Metal Nanoparticles. *ACS Appl. Mater. Interfaces* **2018**, *10*, 14036−14044.
(77) Pawar, S. P.; Gandi, M.; Bose, S. High Performance Electromagnetic Wave Absorbers Derived from PC/SAN Blends

Containing Multiwall Carbon Nanotubes and Fe_3O_4 Decorated onto Graphene Oxide Sheets. *RSC Adv.* **2016**, *6*, 37633−37645.
(78) Srivastava, R. K.; Xavier, P.; Gupta, S. N.; Kar, G. P.; Bose, S.; Sood, A. K. Excellent Electromagnetic Interference Shielding by Graphene- $MnFe_2O_4$-Multiwalled Carbon Nanotube Hybrids at Very Low Weight Percentage in Polymer Matrix. *ChemistrySelect* **2016**, *1*, 5995−6003.
(79) Nath, K.; Ghosh, S.; Ghosh, S. K.; Das, P.; Das, N. C. Facile Preparation of Light-Weight Biodegradable and Electrically Conductive Polymer Based Nanocomposites for Superior Electromagnetic Interference Shielding Effectiveness. *J. Appl. Polym. Sci.* **2021**, *138*, No. 50514.
(80) Gulzar, N.; Zubair, K.; Shakir, M. F.; Zahid, M.; Nawab, Y.; Rehan, Z. A. Effect on the EMI Shielding Properties of Cobalt Ferrites and Coal-Fly-Ash Based Polymer Nanocomposites. *J. Supercond. Novel Magn.* **2020**, *33*, 3519−3524.
(81) Dar, M. A.; Majid, K.; Najar, M. H.; Kotnala, R. K.; Shah, J.; Dhawan, S. K.; Farukh, M. Surfactant-Assisted Synthesis of Polythiophene/$Ni_{0.5}Zn_{0.5}Fe_{2-x}Ce_xO_4$ Ferrite Composites: Study of Structural, Dielectric and Magnetic Properties for EMI-Shielding Applications. *Phys. Chem. Chem. Phys.* **2017**, *19*, 10629−10643.
(82) Yan, D.-X.; Pang, H.; Li, B.; Vajtai, R.; Xu, L.; Ren, P.-G.; Wang, J.-H.; Li, Z.-M. Structured Reduced Graphene Oxide/Polymer Composites for Ultra-Efficient Electromagnetic Interference Shielding. *Adv. Funct. Mater.* **2015**, *25*, 559−566.
(83) Sambyal, P.; Dhawan, S. K.; Gairola, P.; Chauhan, S. S.; Gairola, S. P. Synergistic Effect of Polypyrrole/BST/rGO/Fe_3O_4 Composite for Enhanced Microwave Absorption and EMI Shielding in X-Band. *Curr. Appl. Phys.* **2018**, *18*, 611−618.
(84) Xu, H.; Yin, X.; Li, X.; Li, M.; Liang, S.; Zhang, L.; Cheng, L. Lightweight Ti_2CT_x MXene/Poly(vinyl alcohol) Composite Foams for Electromagnetic Wave Shielding with Absorption-Dominated Feature. *ACS Appl. Mater. Interfaces* **2019**, *11*, 10198−10207.
(85) Saini, P.; Choudhary, V.; Vijayan, N.; Kotnala, R. K. Improved Electromagnetic Interference Shielding Response of Poly(aniline)-Coated Fabrics Containing Dielectric and Magnetic Nanoparticles. *J. Phys. Chem. C* **2012**, *116*, 13403−13412.
(86) Liu, H.; Liang, C.; Chen, J.; Huang, Y.; Cheng, F.; Wen, F.; Xu, B.; Wang, B. Novel 3D network porous graphene nanoplatelets /Fe_3O_4/epoxy nanocomposites with enhanced electromagnetic interference shielding efficiency. *Compos. Sci. Technol.* **2019**, *169*, 103−109104.
(87) Zhang, H.-B.; Yan, Q.; Zheng, W.-G.; He, Z.; Yu, Z.-Z. Tough Graphene-Polymer Microcellular Foams for Electromagnetic Interference Shielding. *ACS Appl. Mater. Interfaces* **2011**, *3*, 918−924.
(88) Shen, B.; Zhai, W.; Tao, M.; Ling, J.; Zheng, W. Lightweight, Multifunctional Polyetherimide/Graphene@Fe_3O_4 Composite Foams for Shielding of Electromagnetic Pollution. *ACS Appl. Mater. Interfaces* **2013**, *5*, 11383−11391.
(89) Zhang, H.; Zhang, G.; Li, J.; Fan, X.; Jing, Z.; Li, J.; Shi, X. Lightweight, multifunctional microcellular PMMA/Fe_3O_4@MWCNTs nanocomposite foams with efficient electromagnetic interference shielding. *Composites, Part A* **2017**, *100*, 128−138.
(90) Ling, J.; Zhai, W.; Feng, W.; Shen, B.; Zhang, J.; Zheng, W. Facile Preparation of Lightweight Microcellular Polyetherimide/Graphene Composite Foams for Electromagnetic Interference Shielding. *ACS Appl. Mater. Interfaces* **2013**, *5*, 2677−2684.
(91) Pawar, S. P.; Biswas, S.; Kar, G. P.; Bose, S. High frequency millimetre wave absorbers derived from polymeric nanocomposites. *Polymer* **2016**, *84*, 398−419.
(92) Chen, D.; Wang, G.-S.; He, S.; Liu, J.; Guo, L.; Cao, M.-S. Controllable Fabrication of Mono-Dispersed rGO−Hematite Nanocomposites and Their Enhanced Wave Absorption Properties. *J. Mater. Chem. A* **2013**, *1*, 5996−6003.
(93) Yan, J.; Huang, Y.; Chen, X.; Wei, C. Conducting Polymers-$NiFe_2O_4$ Coated on Reduced Graphene Oxide Sheets as Electromagnetic (EM) Wave Absorption Materials. *Synth. Met.* **2016**, *221*, 291−298.
(94) Liu, H.; Li, Y.; Dai, K.; Zheng, G.; Liu, C.; Shen, C.; Yan, X.; Guo, J.; Guo, Z. Electrically Conductive Thermoplastic Elastomer Nanocomposites at Ultralow Graphene Loading Levels for Strain Sensor Applications. *J. Mater. Chem. C* **2016**, *4*, 157−166.
(95) Shakir, M. F.; Tariq, A.; Rehan, Z. A.; Nawab, Y.; Abdul Rashid, I.; Afzal, A.; Hamid, U.; Raza, F.; Zubair, K.; Rizwan, M. S.; Riaz, S.; Sultan, A.; Muttaqi, M. Effect of Nickel-Spinal-Ferrites on EMI Shielding Properties of Polystyrene/Polyaniline Blend. *SN Appl. Sci.* **2020**, *2*, No. 706.
(96) Quan, B.; Liang, X.; Ji, G.; Cheng, Y.; Liu, W.; Ma, J.; Zhang, Y.; Li, D.; Xu, G. Dielectric Polarization in Electromagnetic Wave Absorption: Review and Perspective. *J. Alloys Compd.* **2017**, *728*, 1065−1075.
(97) Chen, Y.-J.; Zhang, F.; Zhao, G.-g.; Fang, X.-y.; Jin, H.-B.; Gao, P.; Zhu, C.-L.; Cao, M.-S.; Xiao, G. Synthesis, Multi-Nonlinear Dielectric Resonance, and Excellent Electromagnetic Absorption Characteristics of Fe_3O_4/ZnO Core/Shell Nanorods. *J. Phys. Chem. C* **2010**, *114*, 9239−9244.
(98) Movassagh-Alanagh, F.; Bordbar-Khiabani, A.; Ahangari-Asl, A. Three-Phase PANI@nano-Fe_3O_4@CFs Heterostructure: Fabrication, Characterization and Investigation of Microwave Absorption and EMI Shielding of PANI@nano-Fe_3O_4@CFs/Epoxy Hybrid Composite. *Compos. Sci. Technol.* **2017**, *150*, 65−78.
(99) Xie, A.; Jiang, W.; Wu, F.; Dai, X.; Sun, M.; Wang, Y.; Wang, M. Interfacial Synthesis of Polypyrrole Microparticles for Effective Dissipation of Electromagnetic Waves. *J. Appl. Phys.* **2015**, *118*, No. 204105.
(100) Zhang, Z.; Wang, G.; Gu, W.; Zhao, Y.; Tang, S.; Ji, G. A breathable and flexible fiber cloth based on cellulose/polyaniline cellular membrane for microwave shielding and absorbing applications. *J. Colloid Interface Sci.* **2022**, *605*, 193−203.
(101) Zhang, X.; Qiao, J.; Zhao, J.; Xu, D.; Wang, F.; Liu, C.; Jiang, Y.; Wu, L.; Cui, P.; Lv, L.; Wang, Q.; Liu, W.; Wang, Z.; Liu, J. High-Efficiency Electromagnetic Wave Absorption of Cobalt- Decorated NH_2-UIO-66-Derived Porous ZrO_2/C. *ACS Appl. Mater. Interfaces* **2019**, *11*, 35959−35968.
(102) Wang, L.; Jia, X.; Li, Y.; Yang, F.; Zhang, L.; Liu, L.; Ren, X.; Yang, H. Synthesis and Microwave Absorption Property of Flexible Magnetic Film Based on Graphene Oxide/Carbon Nanotubes and Fe_3O_4 Nanoparticles. *J. Mater. Chem. A* **2014**, *2*, 14940−14946.
(103) Guan, G.; Gao, G.; Xiang, J.; Yang, J.; Gong, L.; Chen, X.; Zhang, Y.; Zhang, K.; Meng, X. $CoFe_2/BaTiO_3$ Hybrid Nanofibers for Microwave Absorption. *ACS Appl. Nano Mater.* **2020**, *3*, 8424−8437.
(104) Yin, Y.; Zeng, M.; Liu, J.; Tang, W.; Dong, H.; Xia, R.; Yu, R. Enhanced High-Frequency Absorption of Anisotropic Fe_3O_4 /Graphene Nanocomposites. *Sci. Rep.* **2016**, *6*, No. 25075.
(105) Ibrahim, I. R.; Matori, K. A.; Ismail, I.; Awang, Z.; Rusly, S. N. A.; Nazlan, R.; Mohd Idris, F.; Muhammad Zulkimi, M. M.; Abdullah, N. H.; Mustaffa, M. S.; et al. A Study on Microwave Absorption Properties of Carbon Black and $Ni_{0.6}Zn_{0.4}Fe_2O_4$ Nanocomposites by Tuning the Matching-Absorbing Layer Structures. *Sci. Rep.* **2020**, *10*, No. 3135.
(106) Li, X.; Shu, R.; Wu, Y.; Zhang, J.; Wan, Z. Fabrication of Nitrogen-Doped Reduced Graphene Oxide/Cobalt Ferrite Hybrid Nanocomposites as Broadband Electromagnetic Wave Absorbers in Both X and Ku Bands. *Synth. Met.* **2021**, *271*, No. 116621.
(107) Zong, M.; Huang, Y.; Zhang, N.; Wu, H. Influence of (rGO)/(ferrite) ratios and graphene reduction degree on microwave absorption properties of graphene composites. *J. Alloys Compd.* **2015**, *644*, 491−501.
(108) Xiong, L.; Yu, M.; Liu, J.; Li, S.; Xue, B. Preparation and evaluation of the microwave absorption properties of template-free graphene foam-supported Ni nanoparticles. *RSC Adv.* **2017**, *7*, 14733−14741.
(109) Liu, X.; Cui, X.; Chen, Y.; Zhang, X.-J.; Yu, R.; Wang, G.-S.; Ma, H. Modulation of electromagnetic wave absorption by carbon shell thickness in carbon encapsulated magnetite nanospindles-poly(vinylidenefluoride) composites. *Carbon* **2015**, *95*, 870−878.

https://doi.org/10.1021/acsomega.1c04192
ACS Omega 2021, 6, 28098−28118

(110) Kim, S.; Oh, J.-S.; Kim, M.-G.; Jang, W.; Wang, M.; Kim, Y.; Seo, H. W.; Kim, Y. C.; Lee, J.-H.; Lee, Y.; et al. Electromagnetic Interference (EMI) Transparent Shielding of Reduced Graphene Oxide (rGO) Interleaved Structure Fabricated by Electrophoretic Deposition. *ACS Appl. Mater. Interfaces* **2014**, *6*, 17647−17653.
(111) Liu, P.; Gao, S.; Zhang, G.; Huang, Y.; You, W.; Che, R. Hollow Engineering to Co@N-Doped Carbon Nanocages via Synergistic Protecting-Etching Strategy for Ultrahigh Microwave Absorption. *Adv. Funct. Mater.* **2021**, *31*, No. 2102812.
(112) Lou, Z.; Han, H.; Zhou, M.; Han, J.; Cai, J.; Huang, C.; Zou, J.; Zhou, X.; Zhou, H.; Sun, Z. Synthesis of Magnetic Wood with Excellent and Tunable Electromagnetic Wave-Absorbing Properties by a Facile Vacuum/Pressure Impregnation Method. *ACS Sustainable Chem. Eng.* **2018**, *6*, 1000−1008.
(113) Liu, Y.; Chen, Z.; Zhang, Y.; Feng, R.; Chen, X.; Xiong, C.; Dong, L. Broadband and Lightweight Microwave Absorber Constructed by in Situ Growth of Hierarchical $CoFe_2O_4$/Reduced Graphene Oxide Porous Nanocomposites. *ACS Appl. Mater. Interfaces* **2018**, *10*, 13860−13868.
(114) Wu, Y.; Pan, W.; Li, Y.; Yang, B.; Meng, B.; Li, R.; Yu, R. Surface-Oxidized Amorphous Fe Nanoparticles Supported on Reduced Graphene Oxide Sheets for Microwave Absorption. *ACS Appl. Nano Mater.* **2019**, *2*, 4367−4376.
(115) Gao, S.; Zhang, G.; Wang, Y.; Han, X.; Huang, Y.; Liu, P. MOFs derived magnetic porous carbon microspheres constructed bycore-shell Ni@C with high-performance microwave absorption. *J. Mater. Sci. Technol.* **2021**, *88*, 56−65.
(116) Zhu, X.; Qiu, H.; Chen, P.; Chen, G.; Min, W. Anemone-Shaped ZIF-67@CNTs as Effective Electromagnetic Absorbent Covered the Whole X-Band. *Carbon* **2021**, *173*, 1−10.
(117) Manna, K.; Srivastava, S. K. Fe_3O_4@Carbon@Polyaniline Trilaminar Core−Shell Composites as Superior Microwave Absorber in Shielding of Electromagnetic Pollution. *ACS Sustainable Chem. Eng.* **2017**, *5*, 10710−10721.
(118) Liu, J.; Che, R.; Chen, H.; Zhang, F.; Xia, F.; Wu, Q.; Wang, M. Microwave Absorption Enhancement of Multifunctional Composite Microspheres with Spinel Fe_3O_4 Cores and Anatase TiO_2 Shells. *Small* **2012**, *8*, 1214−1221.
(119) Zhang, Y.; Wang, X.; Cao, M. Confinedly implanted $NiFe_2O_4$-rGO: Cluster tailoring and highly tunable electromagnetic properties for selective-frequency microwave absorption. *Nano Res.* **2018**, *11*, 1426−1436.
(120) Liu, X.; Zhao, X.; Yan, J.; Huang, Y.; Li, T.; Liu, P. Enhanced electromagnetic wave absorption performance of core-shell Fe_3O_4@poly(3,4-ethylenedioxythiophene) microspheres/reduced graphene oxide composite. *Carbon* **2021**, *178*, 273−284.
(121) Qiao, M.; Lei, X.; Ma, Y.; Tian, L.; He, X.; Su, K.; Zhang, Q. Application of yolk−shell Fe_3O_4@N-doped carbon nanochains as highly effective microwave-absorption material. *Nano Res.* **2018**, *11*, 1500−1519.
(122) Abrisham, M.; Sarmad, M. P.; Sadeghi, G. M. M.; Arjmand, M.; Dehghan, P.; Amirkiai, A. Microstructural design for enhanced mechanical property and shape memory behavior of polyurethane nanocomposites: Role of carbon nanotube, montmorillonite, and their hybrid fillers. *Polym. Test.* **2020**, *89*, No. 106642.
(123) Bera, M.; Prabhakar, A.; Maji, P. K. Nanotailoring of thermoplastic polyurethane by amine functionalized graphene oxide: Effect of different amine modifier on final properties. *Composites, Part B* **2020**, *195*, No. 108075.
(124) Eichner, E.; Heinrich, S.; Schneider, G. A. Influence of particle shape and size on mechanical properties in copper-polymer composites. *Powder Technol.* **2018**, *339*, 39−45.
(125) Menon, A. V.; Madras, G.; Bose, S. Mussel-Inspired Self-Healing Polyurethane with "Flower-like" Magnetic MoS_2 as Efficient Microwave Absorbers. *ACS Appl. Polym. Mater.* **2019**, *1*, 2417−2429.
(126) Marcano, D. C.; Kosynkin, D. V.; Berlin, J. M.; Sinitskii, A.; Sun, Z.; Slesarev, A.; Alemany, L. B.; Lu, W.; Tour, J. M. Improved Synthesis of Graphene Oxide. *ACS Nano* **2010**, *4*, 4806−4814.
(127) Yadav, R. S.; Kuřitka, I.; Vilcakova, J.; Machovsky, M.; Skoda, D.; Urbánek, P.; Masař, M.; Jurča, M.; Urbánek, M.; Kalina, L.; et al. $NiFe_2O_4$ Nanoparticles Synthesized by Dextrin from Corn-Mediated Sol−Gel Combustion Method and Its Polypropylene Nanocomposites Engineered with Reduced Graphene Oxide for the Reduction of Electromagnetic Pollution. *ACS Omega* **2019**, *4*, 22069−22081.

https://doi.org/10.1021/acsomega.1c04192
ACS Omega 2021, 6, 28098−28118